Article

Neuron

# How Diverse Retinal Functions Arise from Feedback at the First Visual Synapse

## Highlights

- Horizontal cells shape the response dynamics of ganglion cells in six distinct ways
- Horizontal cells fulfill distinct functions for different ganglion cell types
- Functions include sharpening and scaling of responses, and enabling delayed responses
- A computational model explains the observed array of horizontal cell functions

## Authors

Antonia Drinnenberg, Felix Franke, Rei K. Morikawa, ..., Andreas Hierlemann, Rava Azeredo da Silveira, Botond Roska

## Correspondence

rava@ens.fr (R.A.d.S.), botond.roska@iob.ch (B.R.)

## In Brief

Interneurons are key actors in the input-output transformations of many brain regions. Combining experiment and theory, Drinnenberg and Franke et al. show how a single interneuron type in the retina shapes the functional diversity of the retinal output.

Drinnenberg et al., 2018, Neuron *99*, 1–18
July 11, 2018 
https://doi.org/10.1016/j.neuron.2018.06.001

CellPress

Please cite this article in press as: Drinnenberg et al., How Diverse Retinal Functions Arise from Feedback at the First Visual Synapse, Neuron (2018), https://doi.org/10.1016/j.neuron.2018.06.001

Neuron
Article



# How Diverse Retinal Functions Arise from Feedback at the First Visual Synapse

Antonia Drinnenberg,[1,2,3,10] Felix Franke,[4,10] Rei K. Morikawa,[1,2] Josephine Jüttner,[1,2] Daniel Hillier,[1,2] Peter Hantz,[1,9] Andreas Hierlemann,[4] Rava Azeredo da Silveira,[5,6,7,*] and Botond Roska[1,2,8,11,*]
[1]Friedrich Miescher Institute for Biomedical Research, 4058 Basel, Switzerland
[2]Institute of Molecular and Clinical Ophthalmology Basel, 4031 Basel, Switzerland
[3]Faculty of Natural Sciences, University of Basel, 4003 Basel, Switzerland
[4]Bio Engineering Laboratory, Department of Biosystems Science and Engineering of ETH Zurich, 4058 Basel, Switzerland
[5]Department of Physics, Ecole Normale Supérieure, 75005 Paris, France
[6]Laboratoire de Physique Statistique, École Normale Supérieure, PSL Research University; Université Paris Diderot Sorbonne Paris-Cité; Sorbonne Universités UPMC Univ Paris 06; CNRS, 75005 Paris, France
[7]Princeton Neuroscience Institute, Princeton University, Princeton, NJ 08544, USA
[8]Department of Ophthalmology, University of Basel, 4031 Basel, Switzerland
[9]Present address: Medical School, University of Pécs, 7624 Pécs, Hungary
[10]These authors contributed equally
[11]Lead Contact
*Correspondence: rava@ens.fr (R.A.d.S.), botond.roska@iob.ch (B.R.)
https://doi.org/10.1016/j.neuron.2018.06.001

## SUMMARY

**Many brain regions contain local interneurons of distinct types. How does an interneuron type contribute to the input-output transformations of a given brain region? We addressed this question in the mouse retina by chemogenetically perturbing horizontal cells, an interneuron type providing feedback at the first visual synapse, while monitoring the light-driven spiking activity in thousands of ganglion cells, the retinal output neurons. We uncovered six reversible perturbation-induced effects in the response dynamics and response range of ganglion cells. The effects were enhancing or suppressive, occurred in different response epochs, and depended on the ganglion cell type. A computational model of the retinal circuitry reproduced all perturbation-induced effects and led us to assign specific functions to horizontal cells with respect to different ganglion cell types. Our combined experimental and theoretical work reveals how a single interneuron type can differentially shape the dynamical properties of distinct output channels of a brain region.**

## INTRODUCTION

Brain regions can be viewed as processing centers that transform the signals from several input channels into signals conveyed by several output channels. The circuits that compute these transformations often contain a diverse set of local interneuron types. How does an interneuron type contribute to the input-output transformations of a given brain region? A way to approach this question is to study how the activity of a given interneuron type affects the activity of the entire set of the region's output channels.

We employed this approach in the mouse retina, where the output channels consist of a diverse set of ganglion cell types (Baden et al., 2016). Large populations of ganglion cells can be recorded simultaneously, and recent experimental progress provides genetic access to individual types of retinal interneurons (Siegert et al., 2012). Experimental knowledge on retinal physiology and circuitry is advanced enough (Masland, 2012) that it is possible to formulate computational models that are sufficiently precise to capture details in the data, but sufficiently general and simple to allow for a qualitative understanding of their mechanisms (Gollisch and Meister, 2010).

In this study, we focus on retinal horizontal cells, which in mice constitute a single interneuron type (Peichl and González-Soriano, 1994). Horizontal cells reside at a strategic position within the visual system, since they act at the first visual synapse between photoreceptors and bipolar cells before the signal is split into parallel channels and, ultimately, gives rise to the responses of ~30 types of ganglion cells. Horizontal cells receive glutamatergic input from photoreceptors; in turn, they deliver feedback inhibition to photoreceptors via a sign-inverting synapse (Kramer and Davenport, 2015).

Previous work used pharmacological manipulations, current injections into horizontal cells (Mangel, 1991), or irreversible genetic perturbations (Chaya et al., 2017; Ströh et al., 2018) to investigate the function of horizontal cells. These studies suggested that horizontal cells contribute to the inhibitory surround of receptive fields, light adaptation, gain control, and color opponency in ganglion cells (Chapot et al., 2017; Thoreson and Mangel, 2012). Ablation of horizontal cells led to an increase of sustained ganglion cell activity, and a change in the membrane potential of horizontal cells was shown to increase or decrease ganglion cell activity, depending on the polarity of the ganglion cell's response to light. However, these approaches provided only limited access to examine how horizontal cells shape the

light responses of ganglion cells, as they lacked cell-type specificity, perturbed horizontal cell activity in only a small retinal area, or did not allow for monitoring how the same ganglion cell responded in the presence and absence of horizontal cell feedback. Therefore, key questions about horizontal cell function remain unanswered. How does horizontal cell feedback shape the dynamics of the retinal output? Are individual ganglion cell types differentially affected? As the retinal circuitry differs for each ganglion cell type, it is possible that horizontal cell feedback has distinct effects on the response properties of different ganglion cell types.

Here, we specifically and reversibly perturbed horizontal cell activity across the entire retina using chemogenetics and combined this perturbation with a system-level and cell-type-specific readout of the retinal output. By performing two-photon calcium imaging of cones in whole-mount retinas, we showed that the chemogenetic perturbation effectively and reversibly blocked the light modulation of the feedback from horizontal cells to cones. To monitor the perturbation-induced changes in the retinal output, we recorded the light-evoked spiking activity in thousands of ganglion cells before, during, and after the perturbation using high-density microelectrode arrays. We uncovered six reversible effects on the time course and the range of ganglion cell responses. Unexpectedly, perturbing horizontal cells suppressed or enhanced the responses of ganglion cells of the same polarity at different epochs of the response, even within the same ganglion cell. By identifying ganglion cell types on the microelectrode array and by performing targeted single-cell recordings, we investigated how the observed effects were distributed among different ganglion cell types. We then formulated a computational model to investigate how horizontal cell feedback can selectively influence different ganglion cells. The model captured the six experimentally observed effects, thus providing a unified picture of the diverse observations. Finally, based on our recordings and the model, we assigned specific functions to horizontal cells with respect to different ganglion cell types. Our combined experimental and theoretical work illustrates how a single site of feedback within a brain region can differentially influence the response dynamics of the region's output channels.

## RESULTS

### Chemogenetic Channel Targeted to Horizontal Cells

To reversibly perturb the activity of horizontal cells, we targeted PSAM$^{L141F\ Y115F}$-GlyR (Magnus et al., 2011) (pharmacologically selective actuator module; PSAM), a chloride-permeable ligand-gated ion channel, to horizontal cells. We injected adeno-associated viruses (AAVs) that conditionally express PSAM into mice that express Cre recombinase in horizontal cells (*Gja10-Cre*) (Siegert et al., 2012). We tested eight different AAVs with distinct serotypes, promoters, and coding sequences to optimize expression in horizontal cells. Efficient and cell-type-specific expression of PSAM was achieved by the systemic administration of AAV Ef1a-DIO-PSAM coated with the PHP.B capsid (Deverman et al., 2016) (Figures 1A–1F and S1). A single intravenous injection led to retina-wide expression of PSAM in horizontal cells of both eyes. In total, 89% ± 3% of horizontal cells expressed PSAM, and 99% ± 1% of PSAM-positive cells were horizontal cells (mean ± SEM; n = 6 mice, n = 352 horizontal cells, n = 316 PSAM-positive cells).

### Efficient and Reversible Perturbation of Horizontal Cell Feedback

To assess if PSAM activation with the ligand PSEM$^{308}$ (PSEM) is efficient in perturbing horizontal cell activity, we examined how the chemogenetic activation affects lateral inhibition from horizontal cells to cones. We targeted the calcium indicator GCaMP6s to cones by injecting the eye subretinally with AAVs that express GCaMP6s under a cone-specific promoter (Figures 1G and 1H). In total, 89% ± 2% of cones expressed GCaMP6s, and 95% ± 2% of GCaMP6s-positive cells were cones (mean ± SEM; n = 3 mice, n = 340 cones, n = 325 GCaMP6s-positive cells).

We then imaged light-evoked calcium signals of individual cone axon terminals under photopic light conditions in whole-mount retinas of *Gja10-Cre* mice (Figure 2), either injected with the GCaMP6s-expressing AAV, but not the PSAM-expressing AAV (control retina; n = 3 mice, n = 228 cone terminals), or injected with both the PSAM-expressing AAV and the GCaMP6s-expressing AAV (PSAM retina; n = 3 mice, n = 256 cone terminals). We imaged the same cone terminals before, during, and after PSEM application (bath-applied at a concentration of 3 μM), and during the subsequent application of the AMPA receptor antagonist NBQX. NBQX blocks the glutamatergic input from cones to horizontal cells and, therefore, prevents horizontal cells from providing lateral inhibition to cones.

We quantified lateral inhibition in individual cone terminals, based on their responses to small and large flashed light spots, by computing a lateral inhibition index (LII; the LII ranges from −1 to 1; it equals 1 when the response to the large spot is completely suppressed by lateral inhibition and it equals 0 when the response to the large spot is not affected by lateral inhibition). In control retinas (Figures 2A–2F), lateral inhibition was not statistically different between non-PSEM (mean of before PSEM application and after PSEM washout) and PSEM conditions (Figure 2F; Table S1A). Subsequent NBQX application strongly decreased lateral inhibition in the same cones (Figure 2F; Table S1B). In contrast, in PSAM retinas (Figures 2G–2L) PSEM strongly decreased lateral inhibition (Figure 2L; Table S1C). Lateral inhibition before PSEM application and after washout of PSEM was not statistically different (Figure 2L; Table S1D). To assess the efficiency of the chemogenetic perturbation, we compared PSEM-induced and NBQX-induced effects in PSAM retinas. The NBQX-induced decrease was only slightly stronger than the PSEM-induced decrease (Figure 2L; Table S1E). The fraction of cones with decreased lateral inhibition was not statistically different between PSEM and NBQX conditions (Figure 2M; Fisher's exact test, p = 0.69; PSEM, 98%; NBQX, 99%), and the cones in which lateral inhibition was decreased by NBQX also showed a PSEM-induced decrease of lateral inhibition (Figure 2N; Spearman correlation coefficient $R$ = 0.76). Together, these results show that the activation of PSAM in horizontal cells with 3 μM PSEM leads to the specific, reversible, and efficient perturbation of the light modulation of horizontal cell feedback to cones.

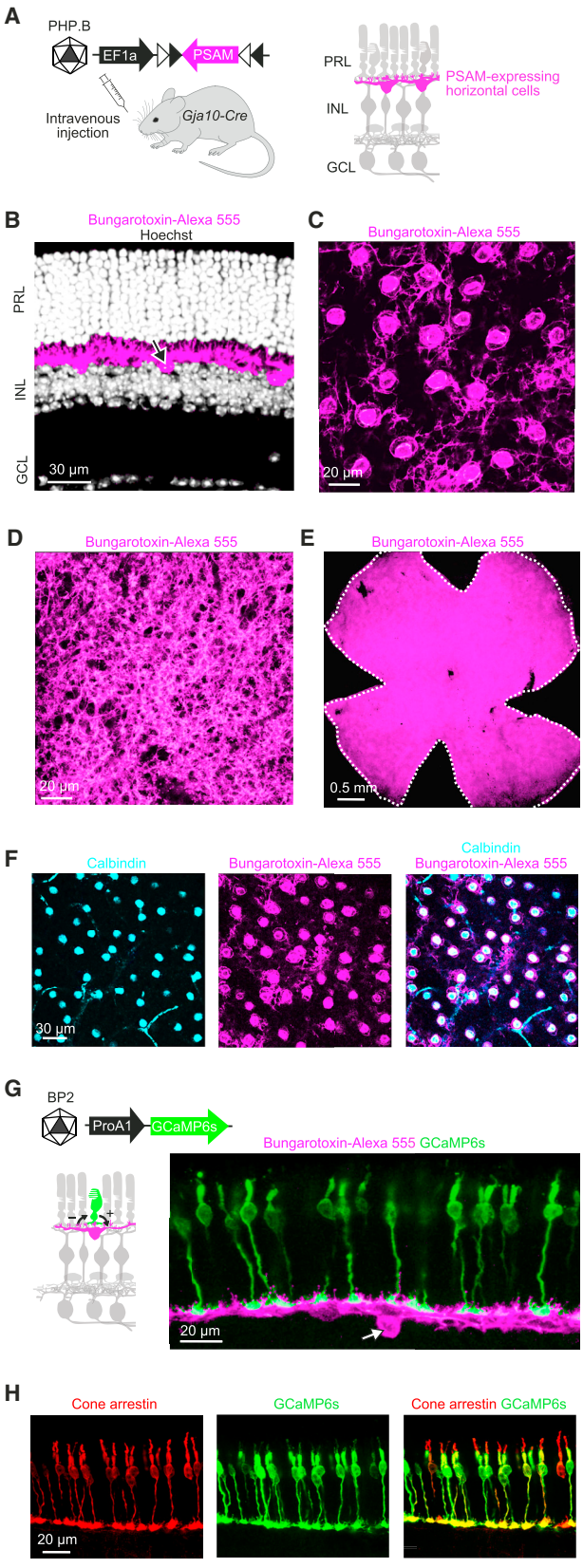


**Figure 1. Chemogenetic Channel PSAM Targeted to Horizontal Cells**

(A) Left: PSAM$^{L141F\ Y115F}$-GlyR (PSAM) was targeted to horizontal cells by injecting mice expressing Cre in horizontal cells (*Gja10-Cre*) intravenously with serotype-PHP.B AAV Ef1a-DIO-PSAM. Right: circuit diagram with horizontal cells (magenta). PRL, photoreceptor layer; INL, inner nuclear layer; GCL, ganglion cell layer.

(B–F) Confocal images of retinas of *Gja10-Cre* mice systemically injected with AAV Ef1a-DIO-PSAM. PSAM was labeled with bungarotoxin-Alexa 555 (magenta). Retinal section (B); top views of INL (C), outer plexiform layer (D), entire retina (E), and INL with horizontal cells labeled with calbindin antibody (cyan) (F). In (B), somata were stained with Hoechst (gray); arrow, soma labeled with bungarotoxin-Alexa 555. White dashed line in (E), outline of retina.

(G) Left: targeting cones by serotype-BP2 AAV ProA1-GCaMP6s (schematic on top). ProA1, cone-specific promoter. Diagram (bottom): sign-conserving (+) and sign-inverting (−) synapses between a cone (green) and a horizontal cell (magenta). Right: confocal image of retinal section of *Gja10-Cre* mouse systemically injected with AAV Ef1a-DIO-PSAM and subretinally injected with AAV ProA1-GCaMP6s. PSAM was labeled with bungarotoxin-Alexa 555 (magenta); GCAMP6s, green. Arrow, soma labeled with bungarotoxin-Alexa 555.

(H) Targeting of cones as in (G); cones were labeled with cone arrestin antibody (red).

See also Figure S1.

## Six Distinct Effects on the Dynamics of Ganglion Cell Responses

How does the perturbation of horizontal cells affect the retinal output? We recorded the light-evoked spiking activity of ganglion cells using high-density microelectrode arrays with >3,000 electrodes/mm$^2$ (Müller et al., 2015) (Figures S2A and S2B). We selected short-wavelength-sensitive cones as the dominant image-forming input by recording from the ventral retina under photopic light conditions. Medium-wavelength-sensitive cones are largely restricted to the dorsal retina (Applebury et al., 2000). Cone dominance of the retinal input under photopic light conditions was shown by direct recordings of rod photoreceptors (Szikra et al., 2014). We monitored the activity of the same ganglion cells before, during, and after PSEM application in retinas of *Gja10-Cre* mice injected with the PSAM-expressing AAV (PSAM retina; n = 29 mice) and in retinas of non-injected *Gja10-Cre* mice (control retina; n = 5 mice). Since cone axon terminals had shown perturbation-induced effects only for large, but not for small, light stimuli (Figures 2I–2K), we initially focused on using large stimuli to study how horizontal cells affect the retinal output. We probed the retina with a sequence of spatially uniform stimuli of different contrasts (Figure S2C).

We analyzed the responses of 6,591 ganglion cells and quantified PSEM-induced effects as the relative change (%) in the spike rate for PSEM versus non-PSEM conditions. We separately examined the responses to light increments ("on-responses") and to light decrements ("off-responses"). We defined ganglion cells that preferentially responded to light increments and light decrements as "ON cells" and "OFF cells," respectively. Moreover, for each light step we divided the responses into an early time window ("transient part of the response," first 0.5 s) and a late time window ("sustained part of the response," last 0.5 s of the 1.86 s duration of the light step). We then categorized ganglion cells based on their responses during the late time window: cells with <5 Hz activity were classified as "transient," while cells with >5 Hz activity were classified as "sustained." Finally, in OFF cells we analyzed

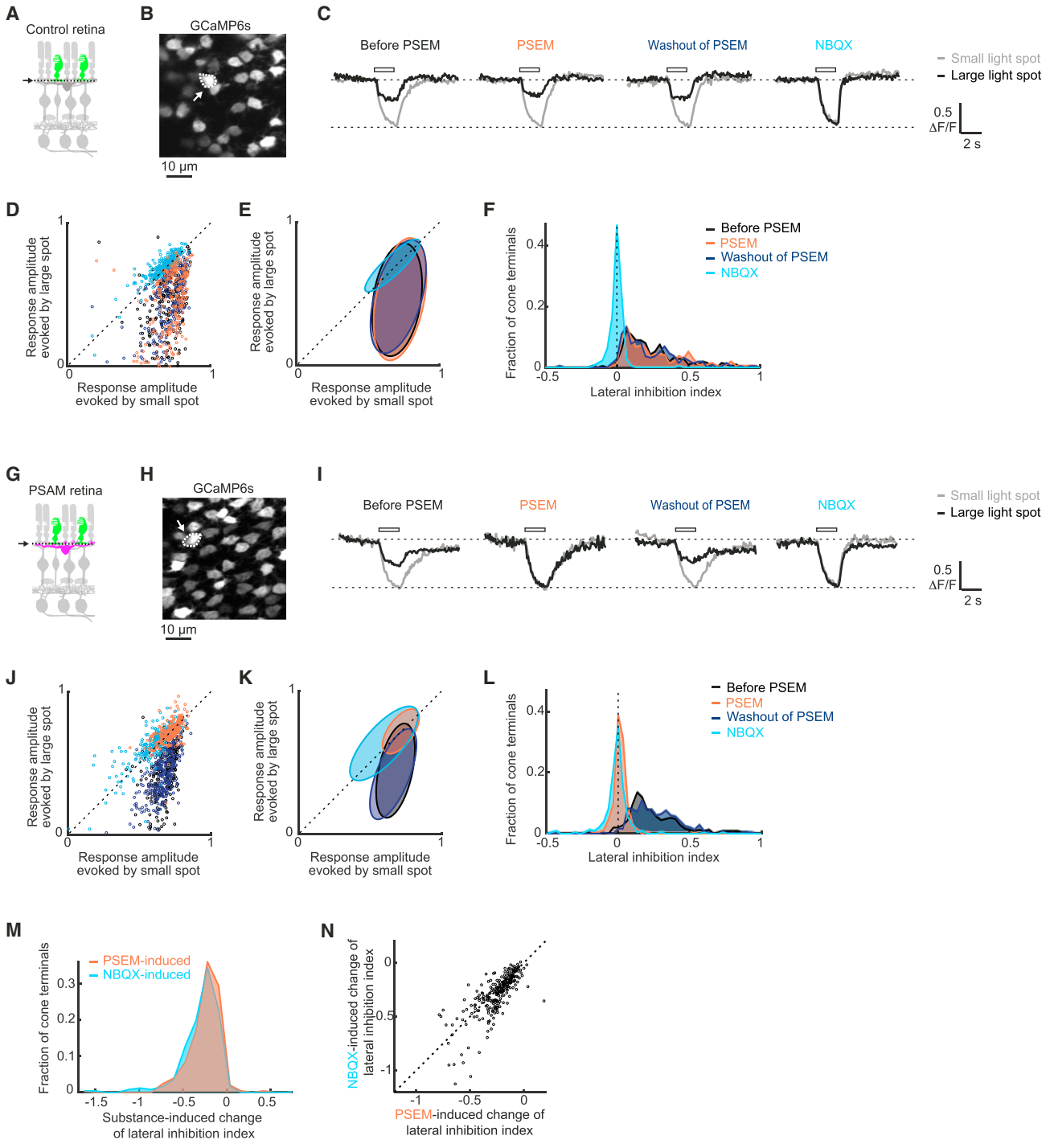


**Figure 2. Reversible Perturbation of Horizontal Cells**

(A) Circuit diagram of retina of *Gja10-Cre* mouse injected with AAV ProA1-GCaMP6s (control retina). Cones expressed GCaMP6s (green). Dashed lines and arrow, imaging plane.

(B) Two-photon image of GCaMP6s-expressing cone axon terminals (top view) in whole-mount control retina. Dashed line and arrow, terminal whose responses are shown in (C).

(C) Example responses of a cone to 120 µm (small) and 3,900 µm (large) flashed light spots. Curves, mean ΔF/F values of three repetitions; white rectangles, stimulus duration. Responses of the same terminal before, during, and after application of PSEM, and during application of NBQX.

(D) Scatterplots of response amplitudes evoked by small (x axis) and large (y axis) spots in control retinas. Data points, individual terminals. Responses of the same terminals are shown for the four conditions.

*(legend continued on next page)*

rebound spiking responses to light increments (''rebound on-response,'' spike rate during 0.5–1.5 s time window after light increments), which are delayed on-responses that frequently occur in OFF cells under photopic light conditions (Tikidji-Hamburyan et al., 2015). In control retinas, we did not detect any significant off-target effects on the overall light-evoked spiking activity of ON cells and OFF cells using 3 μM PSEM (Figure S2D). In the subsequent analysis, we compare PSEM-induced effects between PSAM retinas and control retinas.

We observed six strong and reversible PSEM-induced effects (numbered *i–vi*; Figures 3, S3, and S4; Table S2), which we describe hereafter. ON cells displayed three different effects. First, in transient ON cells, PSEM suppressed the transient part of the on-response (effect *i*, ''transient-on suppression''; Figures 3A and 3G; Table S1F). In total, 25% of transient ON cells showed transient-on suppression in PSAM retinas, whereas in control retinas, this fraction was significantly smaller, 1% (Fisher's exact test, $p = 2.9 \times 10^{-45}$). Second, both in transient and sustained ON cells, PSEM enhanced the sustained part of the on-response (effect *ii*, ''sustained-on enhancement''; Figures 3B and 3H; Table S1G). In total, 13% of transient ON cells and 24% of sustained ON cells showed sustained-on enhancement in PSAM retinas, whereas these fractions were significantly smaller in control retinas: 3.1% and 2.9% (Fisher's exact test, $p = 9.3 \times 10^{-13}$, transient cells; $p = 6.0 \times 10^{-6}$, sustained cells). Interestingly, we observed cases in which transient-on suppression and sustained-on enhancement occurred in the same cell (Figures 3B, S3A, and S3B; 19% of the transient ON cells showing sustained-on enhancement also showed transient-on suppression). Third, in sustained ON cells, PSEM enhanced the on-response over the entire duration of the light increment (effect *iii*, ''all-on enhancement''; Figures 3C and 3I; Table S1H). In total, 24% of sustained ON cells showed all-on enhancement in PSAM retinas, whereas in control retinas this fraction was significantly smaller, 4.3% (Fisher's exact test, $p = 3.3 \times 10^{-5}$).

In OFF cells, we also observed three reversible PSEM-induced effects. First, in transient OFF cells that displayed rebound on-responses (47% of all transient OFF cells), PSEM suppressed the rebound on-responses (effect *iv*, ''rebound-on suppression''; Figures 3D and 3J; Table S1I). This effect was very prevalent: 59% of transient OFF cells with rebound on-responses showed rebound-on suppression in PSAM retinas. In control retinas, this fraction was significantly smaller, 0% (Fisher's exact test, $p = 5.3 \times 10^{-28}$). Second, in the same cells, PSEM enhanced the transient part of the off-response (effect *v*, ''transient-off enhancement''; Figures 3E and 3K; Table S1J). Third, in sustained OFF cells, PSEM suppressed the off-response over the entire duration of the light step in PSAM retinas compared to control retinas (effect *vi*, ''all-off suppression''; Figures 3F and 3L; Table S1K). In total, 13% of sustained OFF cells showed all-off suppression in PSAM retinas, whereas in control retinas this fraction was significantly smaller, 0% (Fisher's exact test, $p = 5.0 \times 10^{-4}$).

Thus, the reversible perturbation of horizontal cells led to an array of diverse and strong effects on the time course of ganglion cell responses. Unexpectedly (Chaya et al., 2017; Mangel, 1991; Ströh et al., 2018), horizontal cell perturbation enhanced or suppressed the responses of ganglion cells of the same polarity at different epochs of the response, even within the same ganglion cell. Within a small area of the retina and at the same time, we found ganglion cells displaying different effects and ganglion cells that were not affected by PSEM (Figure S5), suggesting that the diversity of effects and the lack of effect in some ganglion cells were not due to variations of PSAM expression or the adaptation state of the retina.

## Horizontal Cells Influence the Response Range of Ganglion Cells

Next, we investigated how the response range of ganglion cells was affected by the perturbation of horizontal cells (Figure 4). The response range is the difference between the maximal and minimal spiking response to different contrast steps, and quantifies the cell's ability to encode a range of different contrasts. We found that PSEM significantly compressed the response range of cells that exhibited suppressive PSEM-induced effects, i.e., (*i*) transient-on suppression (Table S1L), (*iv*) rebound-on suppression (Table S1O), and (v*i*) all-off suppression (Table S1Q). In contrast, PSEM significantly expanded the response range of cells that exhibited two of the enhancing PSEM-induced effects, i.e., (*ii*) sustained-on enhancement (Table S1M) and (*v*) transient-off enhancement (Table S1P). The response range of cells exhibiting (*iii*) all-on enhancement was not significantly changed (Table S1N), corresponding to a purely additive effect. These results indicate that horizontal cells can compress or expand the response range of ganglion cells, depending on the polarity and the time window of the response.

## Cell-Type Identification of Ganglion Cells on Microelectrode Arrays

So far we have described how the perturbation of horizontal cells affects the response dynamics of the retinal output by classifying ganglion cells into broad functional categories (i.e., ON, OFF, sustained, and transient). How are individual ganglion cell types affected, and which previously identified ganglion cell type (Farrow et al., 2013) exhibits a given effect? We designed a visual stimulus that allowed us to functionally classify ganglion cells into different types before monitoring how their responses were affected by horizontal cell perturbation. The stimulus was

(E) Two-dimensional Gaussian fits of data in (D). Ellipses, two sigma equiprobability line.
(F) Distributions of lateral inhibition index (LII) in control retinas for the four conditions.
(G) Circuit diagram of retina of *Gja10-Cre* mouse injected with AAV ProA1-GCaMP6s and AAV Ef1a-DIO-PSAM (PSAM retina). Cones expressed GCaMP6s (green), and horizontal cells expressed PSAM (magenta).
(H–L) As in (B)–(F), but for PSAM retinas.
(M) Distributions of PSEM- and NBQX-induced changes in LII value in PSAM retinas.
(N) Scatterplot of PSEM-induced (x axis) and NBQX-induced (y axis) changes in LII values of cones in PSAM retinas.
(D, J, and N) Dashed line, unity line.

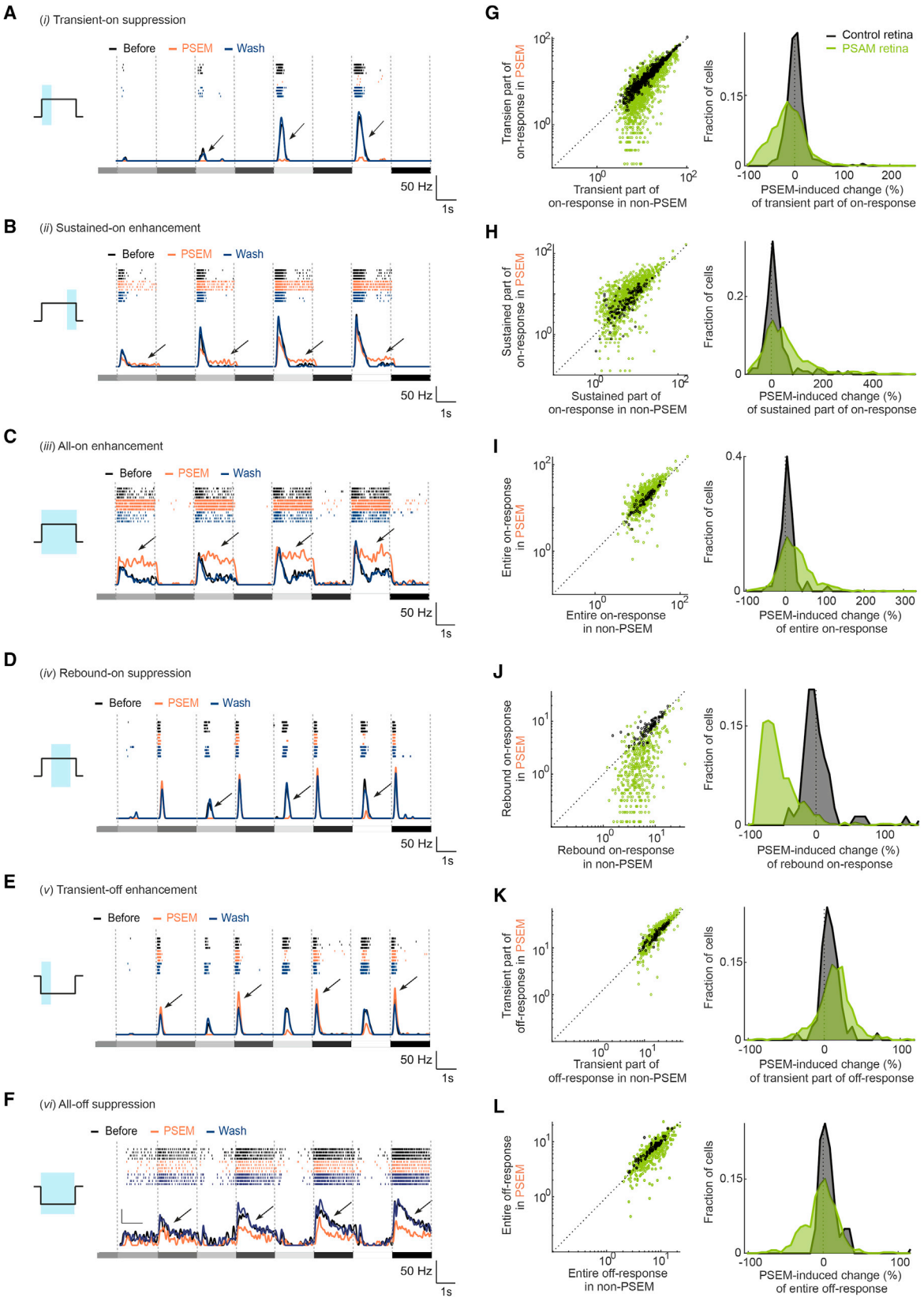


(legend on next page)

designed to meet three criteria: First, it should be short so that it can be used to classify cells before performing horizontal cell perturbation experiments. Second, cells positioned at different retinal locations should be exposed to the same light pattern, without the need of centering the stimulus on individual cells. Third, the stimulus should be naturalistic and rich in visual features. The resulting stimulus included a series of vertical stripes of varying contrast, drifting across the retina at a constant speed along the horizontal axis ("barcode stimulus"; Figures 5A and S6A). The stimulus was short (70 s for six repetitions) and exposed each cell to the same light pattern at different points in time so that the responses of individual cells could later be aligned to each other. Moreover, the stimulus was naturalistic, since the amplitude spectrum of the light intensity along the axis of drift was designed to follow a 1/f distribution (f, spatial frequency), which is typical for natural images (Burton and Moorhead, 1987).

We recorded the spiking responses of ganglion cells to the barcode stimulus using microelectrode arrays (n = 33 mice, n = 12,055 cells). The cells fired bursts of spikes that reliably occurred at distinct time points of the stimulus, which generated a characteristic response pattern in individual ganglion cells (Figure 5A). We performed hierarchical clustering to classify ganglion cells based on their responses to the barcode stimulus and assembled 30 clusters (Figures 5B, 5C, and S6B). Within the clusters, the responses of the cells aligned, creating a pattern that resembled a barcode for a given cluster.

To link the functional clusters obtained using the barcode stimulus to previously characterized ganglion cell types, we developed a method to reveal the genetic identity of ganglion cells during microelectrode array recordings (Figures 5D–5H). We targeted PSAM to a subset of ganglion cells by injecting the eyes of *PV-Cre* mice with AAVs conditionally expressing PSAM under a ganglion cell-specific promoter. In total, 97% of PSAM-expressing cells were restricted to the ganglion cell layer (Figure 5F), and 98% of PSAM-expressing cells were positive for the ganglion cell marker RBPMS (Figure 5E; n = 3 mice, n = 159 PSAM-expressing cells). We identified PSAM-expressing PV ganglion cells on the microelectrode array by selecting the cells whose light-evoked spiking activity was reversibly reduced by PSEM (Figure 5H). Among PV ganglion cells, we focused on PV1, PV5, and PV6 cells by selecting the cells with strong and reliable responses to large spatially uniform stimuli (Farrow et al., 2013; Viney, 2010). We further categorized the cells into PV1 (ON cell, n = 18 cells), PV5 (OFF cell, n = 27 cells), and PV6 (OFF cell, n = 15 cells) cells based on the polarity and the time course of their responses (Figures S6C–S6F). The responses of the PSEM-identified PV1, PV5, and PV6 cells to the barcode stimulus were similar across cells of the same type, but different across cells of different types (Figure 5I; one-way multivariate analysis of variance [MANOVA], $p = 1.4 \times 10^{-7}$). In total, 94% of PSEM-identified PV1 cells were classified to cluster 1, while 80% of PSEM-identified PV6 cells were classified to cluster 14 (Figure 5J). Most PSEM-identified PV5 cells were found in cluster 13 (44%) and cluster 15 (48%). These results indicate that ganglion cells of a given, previously characterized cell type accumulate in the same clusters.

## Horizontal Cells Differentially Affect Individual Ganglion Cell Types

We used the identification of ganglion cell types on the microelectrode array ("on-array" cell-type identification) to investigate how horizontal cells shape the response dynamics of PV1, PV5, and PV6 cells (Figure 6). We further confirmed our findings by performing two-photon laser-targeted single-cell recordings of PV1, PV5, and PV6 cells using patch electrodes in retinas of triple transgenic mice (*Gja10Cre* × *PV-Flp* × *Flp-GFP*-reporter) injected with AAVs conditionally expressing PSAM (Figures 6A–6C). In *Gja10Cre* × *PV-Flp* × *Flp-GFP*-reporter mice, PV1, PV5, and PV6 cells were targeted by selecting GFP-labeled cells with large somata, and further recognized based on their previously described physiological properties (Figures S7A–S7F). On-array-identified ganglion cells of cluster 1 (the cluster to which most PV1 cells were assigned), as well as single-cell recorded, GFP-identified PV1 cells (n = 11 mice, n = 16 cells), displayed sustained-on enhancement (Figures 6D and 6E; Table S1R). On-array-identified ganglion cells of clusters 13 and 15 (the two clusters to which PV5 cells were assigned) and single-cell recorded, GFP-identified PV5 cells (n = 9 mice, n = 17 cells) showed rebound-on suppression (Figures 6F and 6G; Table S1S), combined with transient-off enhancement (Figures 6F and 6H; Table S1T). In on-array-identified ganglion cells of cluster 14 (the cluster to which most PV6 cells were assigned) and in single-cell recorded, GFP-identified PV6 cells (n = 9 mice, n = 10 cells), the rebound-on suppression was present, but less pronounced than in cluster 13/15 (Figures 6I, 6J, and S7G; Tables S1U and S1V), and the transient part of the off-response was suppressed rather than enhanced (Figures 6I, 6K, and S7H; Tables S1W and S1X). These results indicate that horizontal cell perturbation differentially affects individual ganglion cell types.

## Computational Model of Retinal Pathways

The reversible perturbation of horizontal cells led to a catalog of distinct response changes in the retinal output, at different

**Figure 3. Horizontal Cells Shape the Response Dynamics of Ganglion Cells**

(A–F) Spiking activity (top, raster plot, four repetitions per condition; bottom, spike rate, mean values of four repetitions) of individual examples of ganglion cells that preferentially responded to light increments ("ON cells"; A–C) or light decrements ("OFF cells"; D–F), recorded in retinas of *Gja10-Cre* mice injected with AAV Ef1a-DIO-PSAM (PSAM retina). Stimuli: spatially uniform light steps of different contrasts (gray shaded rectangles). Each cell exemplifies one PSEM-induced effect; arrows indicate the effect. Schematic (left) illustrates time window (blue area) with respect to a light step (black line) that was used for quantification in (G)–(L).

(G–L) Left: scatterplots of responses in non-PSEM (refers to the mean value of "before" and "wash") conditions (x axis) and PSEM conditions (y axis) recorded in retinas of non-injected *Gja10-Cre* mice (control, black) or PSAM retinas (green). Data points, individual cells; dashed line, unity line. Right: distributions of PSEM-induced change values (in %) of responses for data shown in left panel.

See also Figures S2–S5 and Tables S1 and S2.

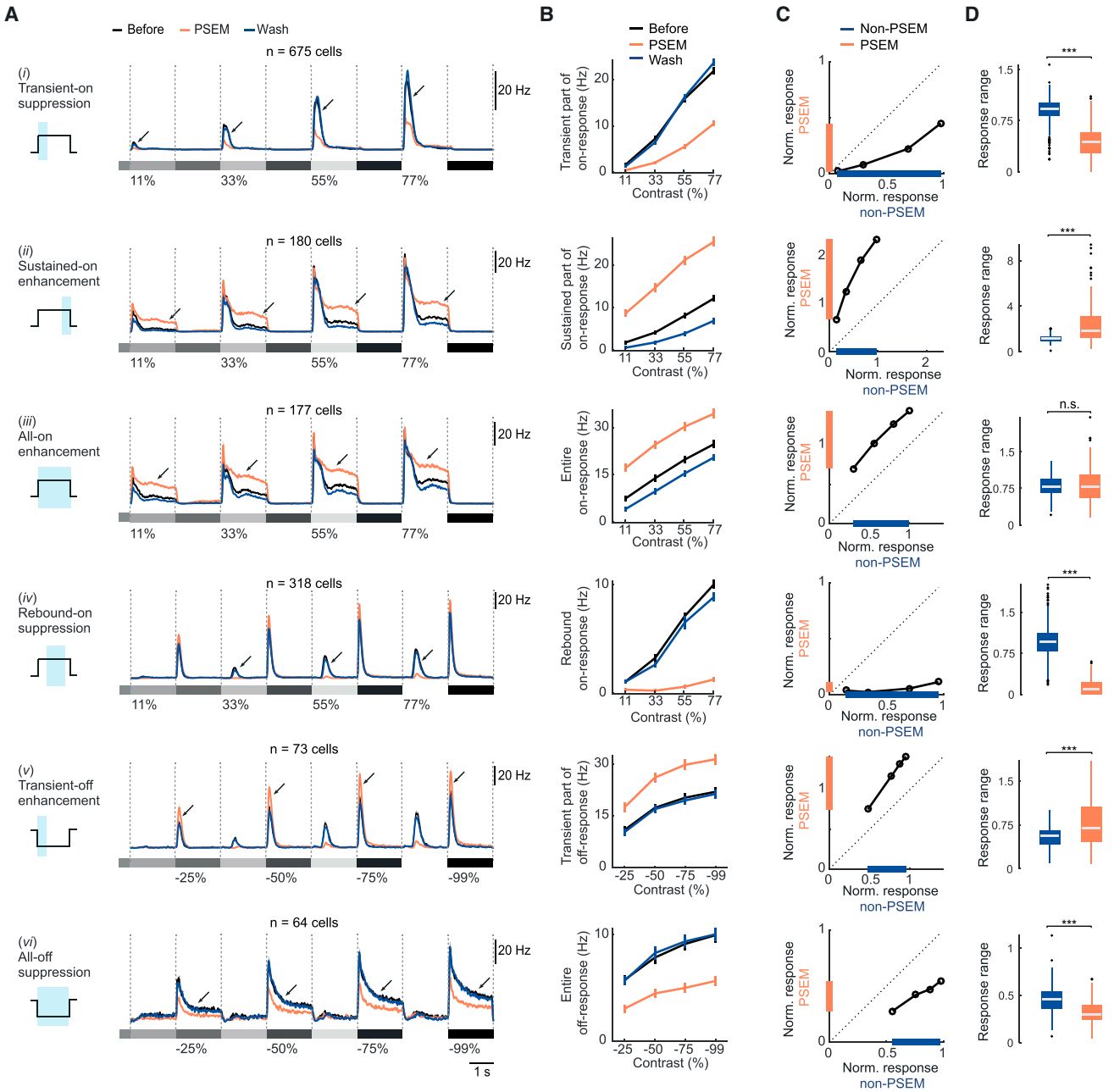


**Figure 4. Horizontal Cells Influence the Response Range of Ganglion Cells**

(A) Each panel: spike rates of PSEM-affected cells for one of the six PSEM-induced effects (numbered *i–vi*; Figure 3). Curves, mean values across cells; shaded areas, ±SEM. Gray shaded rectangles and numbers (%), stimulus contrast; arrows, effects. Schematic (left): time window (blue area) used for quantification in (B)–(D).

(B) Spiking responses (mean spike rate during respective time window) of the cells in (A) plotted against positive (top four panels) or negative (bottom two panels) contrast steps of the stimulus, for each of the six PSEM-induced effects. Curves, mean values; error bars, SEM.

(C) Scatterplots of normalized responses of the cells in (A) in non-PSEM (x axis) and PSEM (y axis) conditions. Data points: responses to each of the four contrast steps, averaged across cells. The response of each cell was normalized to its maximal response in the non-PSEM condition. Colored intervals indicate difference between maximum and minimum of normalized response ("response range") in PSEM (orange) and non-PSEM (blue) condition. Dashed line, unity line.

(D) Boxplot of the distributions of response ranges of PSEM-affected cells. Bottom and top whiskers indicate minima and maxima of data points not considered as outliers, bottom and top of boxes indicate first and third quartiles, central line indicates the median, and black crosses indicate outliers (more than 1.5 times the interquartile range away from the top or bottom of the box). n.s., $p \geq 0.05$, ***$p < 0.001$.

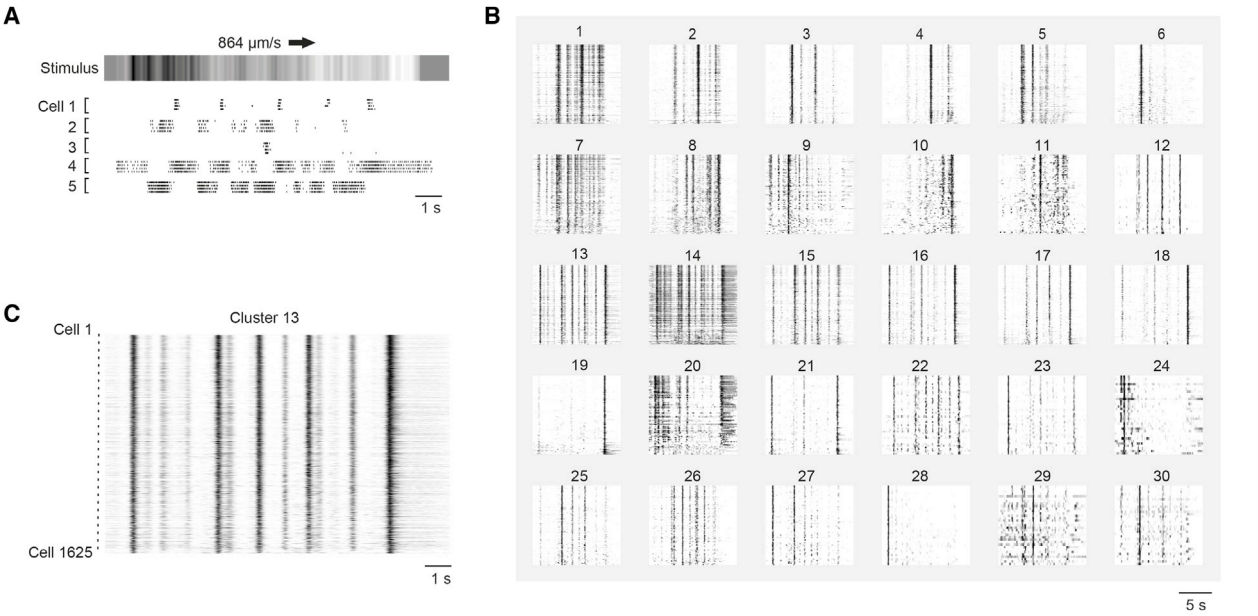


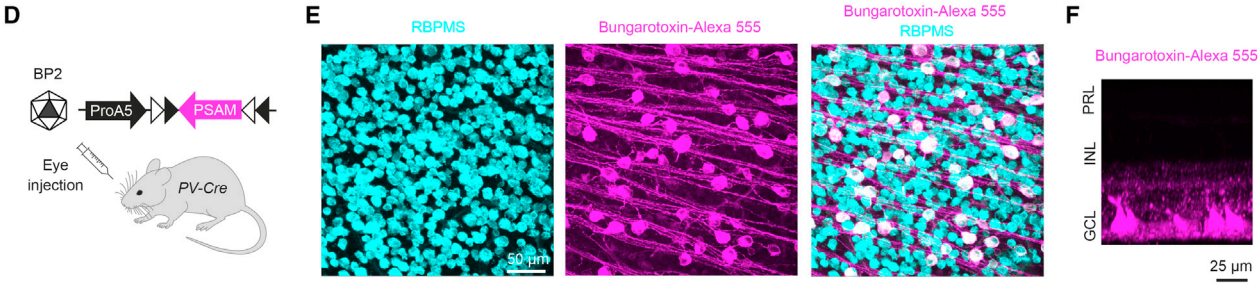


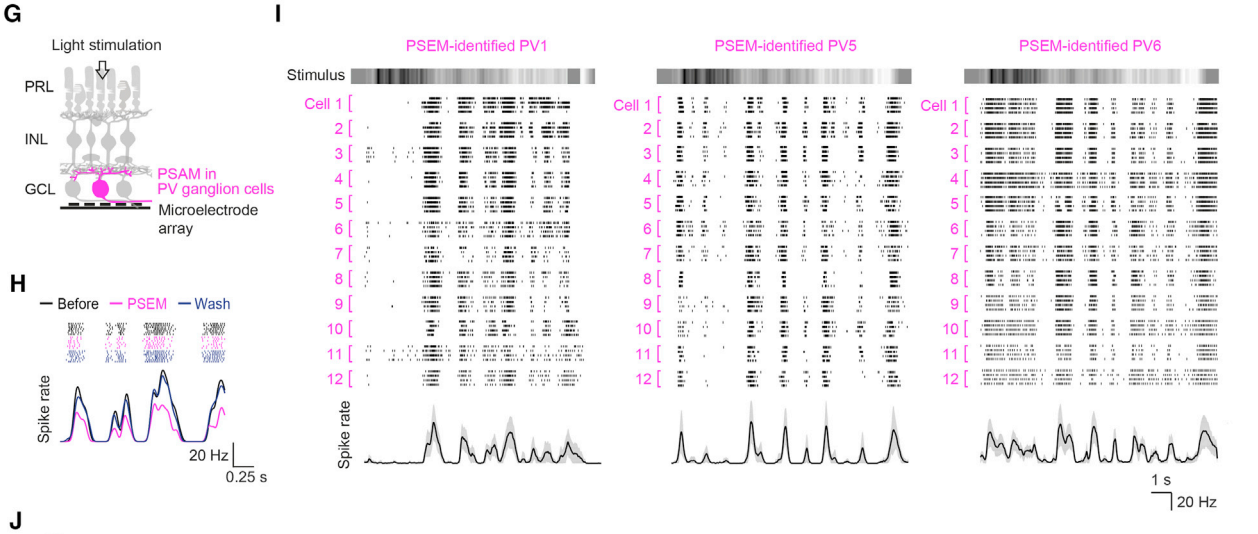


*(legend on next page)*

epochs in the response and in different ganglion cell types. Can our knowledge of the retinal circuitry account for the observed effects? In particular, how can the same interneuron type mediate both response suppression and enhancement in ganglion cells of a given polarity, or even in a single ganglion cell at different time points in its response?

To answer these questions, we constructed a computational circuit model, which related spatially uniform light input to ganglion cell output (Figure 7A). The model consisted of an outer retina component, describing the cone response together with horizontal cell feedback inhibition; an inner retina component, describing the parallel, feedforward processing of the signal; and a ganglion cell component, which received input from the inner retina component and transformed it to spiking activity.

For the outer retina component, we extended earlier models of the cone response (Clark et al., 2013; Szikra et al., 2014), which were supported by data, to include delayed feedback inhibition from horizontal cells. The inner retina component consisted of six parallel, feedforward pathways (Figure 7A), three sign-conserving (OFF) pathways, and three sign-inverting (ON) pathways. Each pathway consisted of a temporal filter and a thresholding unit. The temporal filters were identical for ON and OFF pathways and extracted different temporal properties of the cone response ("fast pathway": narrow biphasic temporal filter, computing an approximate derivative of the cone response; "intermediate pathway": biphasic filter with narrow positive lobe and shallow negative lobe, removing the DC component of the cone output; "slow pathway": monophasic [exponential] filter, smoothing the cone potential and retaining the DC component of the cone output). A model ganglion cell then linearly combined at most two inner retina pathways. An additive contribution corresponded to excitatory input from bipolar cells, while a subtractive contribution corresponded to inhibitory input from bipolar cells through amacrine cells. Finally, the spike rate of a ganglion cell was a function of its combined inputs ("S" in Figures 7A and 7B), in which a single parameter, $\alpha$, controlled how strongly the cell's spike rate was driven directly by the cell's inputs ($\alpha$ close to 0) or by the derivative of the cell's inputs ($\alpha$ close to 1).

## Selective Effects on Model Inner Retina Pathways upon Removal of Horizontal Cell Feedback

We analyzed the model responses of the cone and the inner retina pathways in the presence and absence of horizontal cell feedback (Figures 7C–7E), when the model was stimulated with the spatially uniform light steps of different contrasts that we used in our experiments.

At background light level, a model cone (Figure 7C) was light adapted at a given membrane potential, its "baseline potential." When stimulated with a contrast step, the model cone hyperpolarized in response to light increments and depolarized in response to light decrements. In both cases, the cone response had a transient part, in which the potential reached a peak, followed by a sustained part, in which the potential plateaued at a value different from its baseline. The removal of horizontal cell feedback had several effects on the cone. First, the cone baseline potential was shifted (i.e., hyperpolarized), which shifted the entire response (Figure 7C). Moreover, when deviations from the baseline potential were considered (for illustration purposes, the cone response with subtracted baseline is shown in Figure 7D), two additional effects of the removal of horizontal cell feedback could be identified: the transient part of the cone response was suppressed, and the sustained part was enhanced with respect to the baseline potential. The suppression of the transient part was stronger for responses to light increments with respect to responses to light decrements. This asymmetry was not due to a specific choice of parameters, but originated from the asymmetry of the cone gain adaptation with respect to light increments and decrements, which has been measured experimentally (Clark et al., 2013) and which was captured by the model.

Downstream of the cone, the removal of horizontal cell feedback affected the individual inner retina pathways in distinct ways (Figure 7E). The fast pathways (both ON and OFF) were largely unaffected by the removal of the inhibitory feedback of horizontal cells, as the latter modulated the cone potential only in a delayed manner. The intermediate ON pathway showed a suppression of the transient part and an enhancement of the sustained part of the response upon removal of horizontal cell feedback. These effects occurred because this pathway behaved similarly to the baseline-subtracted, thresholded cone

**Figure 5. Cell-Type Identification on Microelectrode Arrays**

(A) Top: schematic of naturalistic stimulus ("barcode stimulus"). Arrow, stimulus motion. Bottom: raster plot of spiking activity of five example ganglion cells in response to barcode stimulus (four repetitions).

(B) Raster plots of spiking activity of ganglion cells in response to barcode stimulus. Each panel (1–30) shows responses of all cells in one of the 30 clusters.

(C) Close-up of cluster 13.

(D) Schematic of genetic identification of ganglion cell types on microelectrode arrays. *PV-Cre* mice were injected with serotype-BP2 AAV ProA5-DIO-PSAM. ProA5, ganglion cell-specific promoter.

(E) Confocal images (top view) of GCL of retina of these mice (PV-PSAM retina). Ganglion cells were labeled with RBPMS antibody (cyan); PSAM was labeled with bungarotoxin-Alexa 555 (magenta).

(F) Side view of PV-PSAM retina.

(G) Diagram for chemogenetic labeling of PV ganglion cells (magenta) during microelectrode array recordings.

(H) Spiking activity (top, raster plot, seven repetitions per condition; bottom, spike rate, mean values of seven repetitions) of an example ganglion cell in a PV-PSAM retina before, during, and after PSEM application. Stimulus: short natural movie.

(I) Top: schematic of barcode stimulus. Middle: raster plots of responses of twelve example cells recorded in PV-PSAM retinas, whose spiking was reversibly reduced by PSEM. PV1 (left column of panels), PV5 (center), or PV6 (right) cells were identified based on their responses to light steps of different contrast (Figure S6). Bottom: spike rate (black, mean values; gray areas, ±SD).

(J) Distributions of PSEM-identified PV1, PV5, and PV6 cells over the clusters obtained using the barcode stimulus.

See also Figure S6.

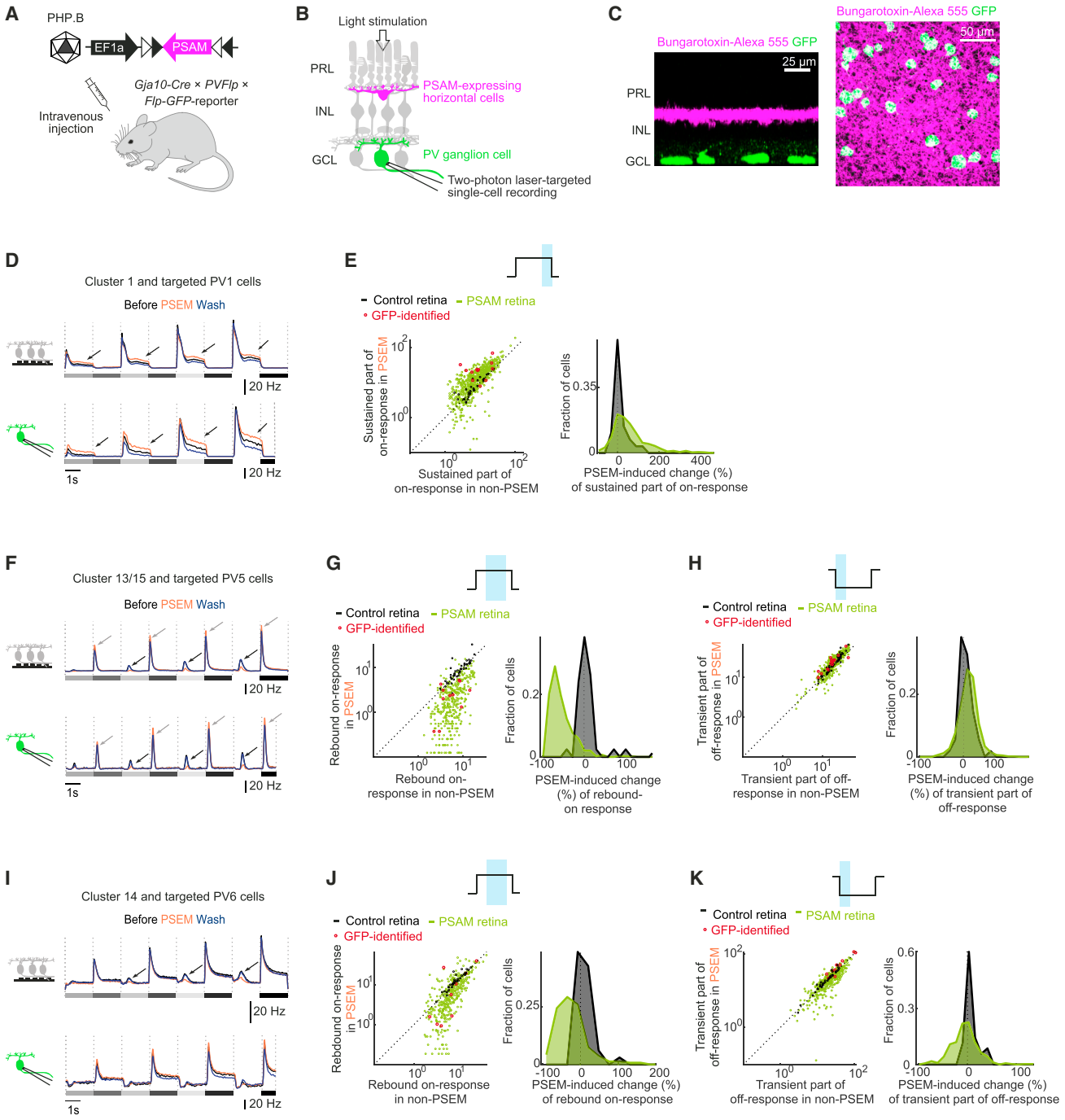


**Figure 6. Horizontal Cells Differentially Affect Individual Ganglion Cell Types**

(A) Retinas of *Gja10Cre* × *PV-Flp* × *Flp-GFP*-reporter mice, systemically injected with AAV Ef1a-DIO-PSAM, express PSAM in horizontal cells and GFP in PV ganglion cells (PV-labeled PSAM retinas; Figure S7).

(B) Schematic for targeted single-cell recording in PV-labeled PSAM retinas.

(C) Confocal images of PV-labeled PSAM retinas (left, side view; right, top view). PSAM was labeled with bungarotoxin-Alexa 555 (magenta); GFP, green.

(D) Top: spike rates of cells in cluster 1 recorded with microelectrode arrays (schematic top left). Bottom: targeted single-cell spike recordings (schematic bottom left) of PV1 cells in PV-labeled PSAM retinas. Curves, mean values; shaded areas, ±SEM. Arrows, PSEM-induced effects; gray shaded rectangles, stimulus contrast (same stimulus as in Figure 3).

(E) Left: scatterplot of responses in non-PSEM (x axis) and PSEM (y axis) conditions. Data points: individual cells of cluster 1, in control retinas (black) or PSAM retinas (green), and targeted single-cell recordings of PV1 in PV-labeled PSAM retinas (red). Schematic (top): time window (blue area) used for quantification. Only

*(legend continued on next page)*

potential and, therefore, inherited all effects of the cone except for the baseline shift. The effects were much weaker in the intermediate OFF pathway because of the asymmetry in the cone response. The slow pathways displayed an overall enhancement (ON pathway) or suppression (OFF pathway) of the response because their responses amounted to the smoothed, thresholded cone response and, therefore, retained information about the baseline shift of the cone potential. Thus, depending on the temporal filter and threshold non-linearities of the inner retina pathways, distinct effects of the feedback removal in the outer retina are selectively passed on to the ganglion cells.

## The Model Captures All Six Perturbation-Induced Effects

We examined the ways in which the output of model ganglion cells was affected by the removal of the horizontal cell feedback. We constructed a set of model ganglion cells (Figure 7F) by combining different inner retina pathways and by varying parameter $\alpha$. The model ganglion cells reproduced qualitatively the measured ganglion cell responses and, remarkably, all six effects that we had observed experimentally during the reversible perturbation of horizontal cells (effects *i–vi*; compare Figures 3A–3F with Figure 7F). Hereafter, we explain how the six effects emerged in different model ganglion cells.

(*i*) Transient-on suppression and (*ii*) sustained-on enhancement were shown by model ganglion cells driven by the intermediate ON pathway, which displayed these effects. The two effects could occur in the same model ganglion cell or occurred in separate cells, depending on parameter $\alpha$: a model ganglion cell whose spike rate strongly depended on the derivative of its inputs ($\alpha$ close to 1) would not have any sustained response in the presence or absence of horizontal cell feedback (effect *i*), whereas a model ganglion cell with $\alpha$ close to 0 would exhibit a sustained response, which was enhanced upon the removal of horizontal cell feedback (effect *ii*). (*iii*) All-on enhancement was displayed by model ganglion cells that received input from a combination of pathways that included the slow ON pathway, as these cells inherited the overall response enhancement that the slow ON pathway displayed upon feedback removal. (*iv* and *v*) Rebound-on suppression and transient-off enhancement were displayed by model ganglion cells that were excited by the fast OFF pathway, that were inhibited by the intermediate ON pathway, and whose spike rate strongly depended on the derivative of their inputs ($\alpha$ close to 1). In the presence of horizontal cell feedback, the rebound on-response was elicited by the fast decay of the inhibitory input from the intermediate ON pathway. The transient off-response was elicited by two factors: the excitatory input from the fast OFF pathway and the removal of inhibition from the intermediate ON pathway at light decrements. In the absence of horizontal cell feedback, rebound-on suppression (effect *iv*) and transient-off enhancement (effect *v*) were caused by the changes of the intermediate ON pathway: as the transient response of the intermediate ON pathway was suppressed while its sustained response was enhanced, the decay of the inhibitory input was slowed down and, therefore, no rebound on-response was elicited (effect *iv*). Moreover, since the sustained response of the intermediate ON pathway was enhanced, a larger inhibitory input from the ON pathway was removed at a light decrement, yielding a larger transient off-response (effect *v*), although the excitatory input from the fast OFF pathway remained unchanged. The model therefore suggested that effects *iv* and *v* share the same mechanism in the inner retina, which can explain why we observed effect *iv* and effect *v* in the same cells (Figures 3D and 3E). (*vi*) All-off suppression was exhibited in model ganglion cells that received input from a combination of pathways that included the slow OFF pathway, as these cells inherited the overall response suppression that the slow OFF pathway displayed upon feedback removal. (*vii*) Finally, model ganglion cells that mainly received input from the fast pathways were not affected by the removal of horizontal cell feedback.

Thus, the model provided insights into how horizontal cell feedback can differentially shape the response dynamics in distinct retinal output channels. Depending on their temporal properties and non-linearities, the inner retina pathways extracted different temporal components of the cone response, which ultimately shaped the time course of the ganglion cell responses: namely, the derivative of the cone response (maximum at 30–90 ms after the light step, depending on contrast); the cone response itself (220–310 ms); the decay of the transient cone response, which caused the rebound on-response in OFF cells (430–500 ms); the plateau of the cone response (>1 s); and finally, the baseline shift of the cone response.

Beyond the first-order effects (*i–vi*), how does the change in the ganglion cell response upon the removal of horizontal cell feedback itself vary with stimulus strength? Answering this question revealed how the response range of a ganglion cell depends on the horizontal cell feedback. We found that the model captured, qualitatively and in some cases quantitatively, all effects of PSEM on the response range of ganglion cells that we had observed experimentally (Figures 8A and 8B). Specifically, the response range was compressed in the model whenever it was compressed in the data, and it was expanded whenever it was expanded in the data.

## New Model Predictions and Their Experimental Validation

The model led to predictions on the effect of the horizontal cell perturbation on the retinal output, four of which we tested in subsequent experiments and analyses (Figures 8C–8G).

First, the most prevalent effect of perturbing horizontal cells experimentally was the suppression of the rebound on-response in transient OFF cells (effect *iv*). The model explained this effect by a slower decay of the inhibitory input from the intermediate ON pathway upon removal of horizontal cell feedback.

cells with responses >2 Hz before PSEM application are shown. Dashed line, unity line. Right: distributions of PSEM-induced relative changes (%) of responses for the data recorded with microelectrode arrays in left panel.

(F–K) As in (D) and (E), but for cells of cluster 13/15 and targeted PV5 cells (F–H), and for cells of cluster 14 and targeted PV6 cells (I–K).

See also Figure S7.

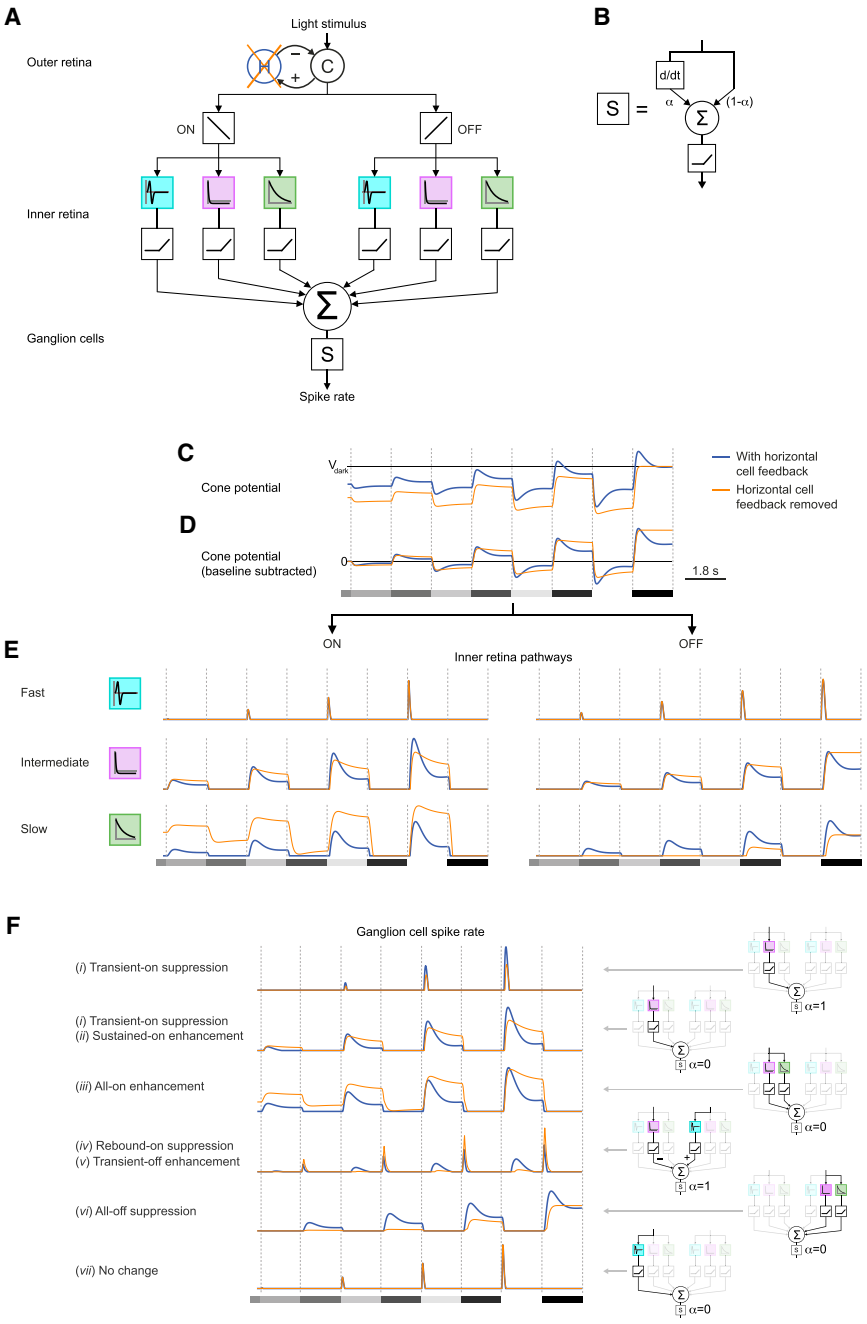


**Figure 7. Computational Model of the Retinal Circuitry Explains All Perturbation-Induced Effects**

(A) Schematic of retinal circuit model. From top to bottom: cone (C)-horizontal cell (H) negative feedback circuit, subsequent split into ON (left) and OFF pathways (right), followed by filtering operations (colored boxes) and threshold non-linearities (black boxes) of inner retina pathways. Removal of horizontal cell feedback, orange cross. For each model ganglion cell, the inner retina pathways were linearly combined (Σ) and converted to a spike rate by function S.

(B) Function S was the thresholded weighted average (Σ, weighted by parameter α) of a ganglion cell's previously combined inputs (right) and the temporal derivative thereof (left, d/dt).

(C) Model cone potential in presence (blue) and absence (orange) of horizontal cell feedback in response to stimulus used in Figure 3 (gray shaded rectangles in D). $V_{dark}$, cone potential in darkness.

(D) Cone potentials with baseline subtracted.

(E) Responses of the six inner retina pathways after the thresholding non-linearity to same stimulus as in (D).

(F) Left: spike rates of six model ganglion cells reproducing the effects observed in data (Figure 3; *i–vi* and cell not affected by PSEM). Right: diagrams depicting the combination of inner retina pathways and parameter α used for each model ganglion cell.

response to light increments in PV5 cells (Viney, 2010), these findings were consistent with the model prediction.

Second, in the model, removal of horizontal cell feedback suppressed the transient part of the response in the intermediate ON pathway, but not in the fast ON pathway. Consistent with the model, in our experiments we found that ON cells that rapidly reached the peak of their response with respect to the stimulus onset displayed a weaker suppression of the transient part of the response compared to ON cells that responded slower (Figures 8E; Table S1Z). The fraction of cells in which PSEM suppressed the transient part of the on-response was 32% for slow-responding cells, while this fraction was significantly lower for fast-responding cells, 9.2% (Fisher's exact test, $p = 1.5 \times 10^{-42}$). Thus, horizontal cells influenced ganglion cells that carry fast signals to a lesser extent than those that carry slow signals.

Third, due to the asymmetry of the gain adaptation in the model cone response, model ganglion cells that received input from the intermediate ON pathway exhibited stronger suppression of their transient responses as compared to model cells that received input from the intermediate OFF pathway. Therefore, the model predicted that, among ganglion cells that are

Since PV5 cells exhibited rebound-on suppression (Figures 6F and 6G), we targeted PV5 cells in *Gja10Cre* × *PV-Flp* × *Flp-GFP*-reporter mice injected with AAVs conditionally expressing PSAM (n = 3 mice, n = 3 cells) and performed cell-attached and whole-cell patch-clamp recordings. Spiking responses of PV5 cells displayed strong rebound on-responses, which were suppressed by PSEM (−85% ± 8%, median ± SEM, PSEM-induced change; Figure 8C). The same cells received transient inhibition with fast decay in response to light increments, which decayed slower in PSEM (Figures 8C and 8D; Table S1Y). Together with the previously reported lack of excitation in

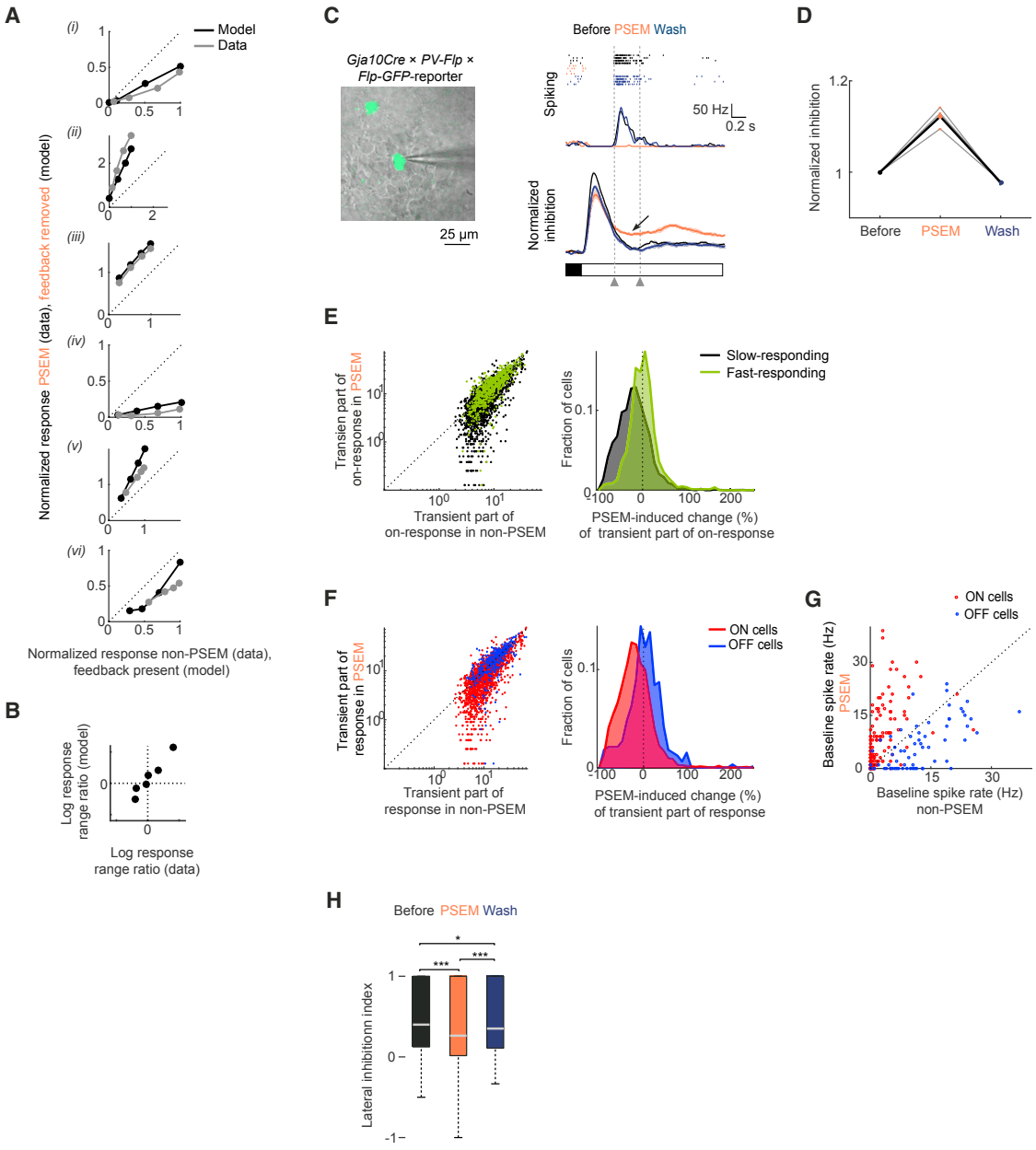


**Figure 8. Experimental Validation of Model Predictions**

(A) Each panel: scatterplot of responses of PSEM-affected cells in non-PSEM (x axis) and PSEM (y axis) conditions ("data"; replotted from Figure 4C) and of response of corresponding model ganglion cell from Figure 7F in presence (x axis) and absence (y axis) of horizontal cell feedback ("model") for one of the six effects *i–vi*. Data points: response to each contrast steps. Each cell's response was normalized to the maximal response in non-PSEM conditions (data), or to the maximal response in presence of horizontal cell feedback (model). Dashed line, unity line.

(B) Scatterplot of logarithm of ratio of recorded response ranges in non-PSEM and PSEM conditions ("data"; x axis), and logarithm of ratio of model response ranges in presence and absence of horizontal cell feedback ("model"; y axis). Each point is one of the six effects.

(C) Targeted patch-clamp recordings of PV5 cells in PV-labeled PSAM retinas. Left: overlay of two-photon image of a GFP-labeled cell (green) and infrared image of GCL and recording pipette (gray). Right: spiking activity (raster plot, four repetitions per condition, and spike rate, mean values of four repetitions) and inhibitory input (normalized to pre-stimulus levels, bottom) of a PV5 cell. Curves, mean values across stimulus repetitions; shaded areas, ±SEM. Shaded rectangles (bottom), stimulus contrast; arrow, slowly decaying inhibitory input during PSEM application; dashed lines, time window used for quantification in (D).

(D) Normalized inhibitory input to PV5 cells recorded in PV-labeled PSAM retinas. Gray lines, data from individual cells; black lines, mean.

(E) Left: scatterplots of transient on-responses of transient ON cells in non-PSEM (x axis) and PSEM (y axis) conditions in PSAM retinas. Data points: responses of individual fast-responding (green) and slow-responding (black) cells. Right: distributions of PSEM-induced relative changes (%) of transient part of on-response for data in left panel.

(F) Same as for (E), but for slow-responding transient ON (red) and OFF (blue) cells.

*(legend continued on next page)*

dominated by inputs from the intermediate pathways, ON cells would display a stronger suppression of the transient part of the response than OFF cells. To test this prediction, we focused on slow-responding transient ganglion cells in our recordings because these cells were dominated neither by the slow pathways (those would be sustained) nor by the fast pathways (those would be fast-responding). Consistent with the prediction, in our experiments we found that PSEM suppressed the transient part of the response more strongly in slow-responding transient ON cells than in slow-responding transient OFF cells (Figure 8F; Table S1AA).

Fourth, model ganglion cells that displayed all-on enhancement or all-off suppression received input from the slow pathways, which were sensitive to the baseline shift in the cone potential due to the removal of horizontal cell feedback. Therefore, the model predicted that ganglion cells that exhibited either of these two effects would display changes in their spontaneous spiking activity during background light stimulation ("baseline spiking activity"). In our experiments, we found that PSEM increased the baseline spike rate in ON cells displaying all-on enhancement (Figure 8G; Table S1BB), while PSEM decreased the baseline spike rate in OFF cells displaying all-off suppression (Figure 8G; Table S1CC), which was consistent with the model prediction.

The model explained the effects at the ganglion cell level based on changes in the dynamics of the cone potential, i.e., a reduction of the temporal modulation of the cone response to a contrast step and a shift of the cone baseline potential (Figures 7C and 7D). To compare the model cone potential with the experimentally measured GCaMP6s signals in cone axon terminals (Figures S8A–S8D), we convolved the potential of the model cone with the impulse function of GCaMP6s. We found that the dynamics of the measured GCaMP6s response to a sequence of contrasts steps was similarly affected by the perturbation of horizontal cells as the dynamics of the modeled calcium signals (Figure S8A). The effects of PSEM on the cone response were qualitatively similar for all contrast steps. We deconvolved the measured GCaMP6s responses to a single contrast step with the GCaMP6s impulse function. Consistent with the model, PSEM reduced the temporal modulation of the deconvolved cone response (Figures S8C and S8D; Table S1DD). Furthermore, PSEM decreased the baseline calcium level of cones (Figures S8E and S8F; Tables S1EE and S1FF), which was consistent with a hyperpolarizing shift of the cone baseline potential as suggested by the model.

### Contribution of Horizontal Cells to the Spatial Processing of Ganglion Cells

So far, we had investigated how horizontal cells influence the time course of ganglion cell responses. Since spatial processing is one of the main suggested functions of horizontal cells, we tested if their reversible perturbation affects the inhibitory surround of ganglion cell receptive fields. We quantified lateral inhibition in ganglion cells in PSAM retinas (n = 3 mice, n = 447 cells) based on their spiking responses to small and large flashed light spots. PSEM led to an LII decrease of 0.08, which corresponds to a 15% decrease in lateral inhibition (Figure 8F; Table S1GG). The change in the LII was not significantly different across the functional clusters obtained using the barcode stimulus (Figure S8G; one-way ANOVA; no pairwise test on the difference of the mean PSEM-induced LII change between two clusters was significant at $p < 0.05$ after Tukey-Kramer correction for multiple testing). Thus, at photopic light levels and in response to large flashed stimuli (Ströh et al., 2018), lateral inhibition from horizontal cells contributes on average to less than a sixth of the strength of the inhibitory surrounds of ganglion cell receptive fields. This finding indicates that, under the conditions of our experiments, amacrine cells are the major contributors to the receptive field surrounds of ganglion cells (Cook and McReynolds, 1998; Franke et al., 2017).

## DISCUSSION

### How Diverse Retinal Functions Arise from Feedback at the First Visual Synapse

This study investigates how a single interneuron type, horizontal cells, affects the dynamics of the output channels of a brain region, the retina. By combining experimental and theoretical approaches, we show how feedback at the first visual synapse can influence the retinal output in distinct ways, by enhancing or suppressing ganglion cell activity during different epochs of the response and in different subsets of ganglion cells. What is the functional relevance of the observed effects? Below we propose three functional roles of horizontal cells, which apply to different subsets of ganglion cells.

First, horizontal cells can induce temporal sharpening of the response of ganglion cells by exerting two different effects in the same ganglion cells (effect *i* and effect *ii* occurring in the same ON cells; Figures 3B, S3A, and S3B). In these cells, horizontal cells sharpened the temporal profile of the response by enhancing the transient part and suppressing the sustained part of the response. Our computational model provided insights into how both effects can arise from a single site of negative feedback. The suppression of the sustained response is a simple consequence of the delayed feedback inhibition from horizontal cells. The enhancement of the transient response, however, is more interesting: generally, temporal sharpening is accompanied by gain suppression—a phenomenon referred to as the "gain-bandwidth trade-off" (Seung, 2002). By contrast, we found that the temporal sharpening was accompanied by a larger (transient) gain. According to the model, this phenomenon

(G) Scatterplot of mean spike rate during background light stimulation ("baseline spike rate") in ON cells displaying all-on enhancement (red) and in OFF cells displaying all-off suppression (blue).
Dashed line in (E)–(G), unity line.
(H) Boxplot of distributions of LII values of ganglion cells. Bottom and top whiskers indicate minima and maxima of data points not considered as outliers, bottom and top of boxes indicate first and third quartiles, central line indicates the median, and black crosses indicate outliers (more than 1.5 times the interquartile range away from the top or bottom of the box). ***$p < 0.001$, n.s., $p \geq 0.05$.
See also Figure S8.

is a direct outcome of non-linear processing in the retina: horizontal cell feedback modulates both the cone baseline potential and its dynamics, and downstream non-linearities couple the two to yield an enhanced transient response. As such, the model illustrates how negative feedback in the outer retina can enhance responses at the retinal output level without invoking a positive feedback mechanism of horizontal cells in the outer retina (Jackman et al., 2011).

Second, horizontal cells influence the response range of the retinal output, as their activity can lead to a compression (effects *ii* and *v*) or an expansion (effects *i*, *iv*, and *vi*) of the response range of ganglion cells, at different epochs of the response (Figures 4C and 4D). We observed response range compression only in a minority of the cases (253/1,487 of cells showing one of the effects *i–vi*; Figures 4C and 4D), even though compression of the response range is the effect expected from feedback inhibition. In the majority of cases (1,057/1,487 of cells showing one of the effects *i–vi*; Figures 4C and 4D), we found that horizontal cell activity led to an expansion of the response range, which was unexpected. The expansion was large for effect *i* (response range expanded by a factor of two) and effect *iv* (response range expanded by a factor of ten). The model captured the observed effects on the response range (Figures 8A and 8B). It also indicated that different mechanisms may underly these effects: response range expansion or compression can derive from the combined action of a delayed inhibitory feedback onto cones together with downstream non-linearities (effect *i*); from the combined action of a shift in the cone baseline potential (the DC component of the cone activity) together with downstream non-linearities (effect *vi*); or from a rebound response caused by the rapid decay of an inhibitory input to ganglion cells, due to the horizontal cell feedback onto cones (effect *iv*).

Third, horizontal cells endow the retina with a ''memory'' of light increments by enabling delayed rebound spiking responses to light increments in a large fraction of transient OFF cells (effect *iv*; Figures 3D and 3J). Compared to the activity of sustained ON cells, which simply follow the light input (i.e., after a light increment, they rapidly stop spiking in response to a subsequent light decrement), the rebound-on response occurs after the light increment with a latency of ~0.5 s, independent of the momentary light input. As such, the rebound spiking enables the cell to ''memorize'' that a light increment occurred ~0.5 s ago. Interesting phenomena could arise if a light decrement occurs shortly after the light increment, and consequently, the rebound-on response starts to overlap, or even coincides with, the transient off-response. The interaction of the two responses results in a temporal tuning of transient OFF cells with a peak at a frequency of ~2 Hz. Furthermore, when a bright object is moved across the receptive field of the cell, the rebound on-response to the leading edge can coincide with the transient OFF response to the trailing edge. This mechanism yields response tuning to a fixed ratio between size and velocity of the moving object.

### How a Single Site of Feedback Can Shape the Circuit's Outputs in Diverse Ways

In our circuit model, the horizontal cell's ability to differentially shape the responses of individual retinal output channels results from the dynamical, non-linear processing of the signal through parallel channels. While in linear systems the response to an input consisting of components with different timescales is the sum of the responses to each of the individual components, this does not apply to non-linear systems: non-linearities can couple different timescales that are present in the signal. For example, in the presence of thresholding non-linearities, a baseline shift can affect the dynamics by rendering the response more or less sustained. Thus, simple non-linearities, combined with the presence of parallel pathways acting on different timescales, can give rise to a rich set of behaviors.

Our work illustrates the unexpected ways in which a neuron in a non-linear circuit can influence the circuit's outputs. First, consistent with our whole-cell patch data (Figures 8C and 8D), the model explains the horizontal cell-driven suppression of the transient response in OFF cells (effect *v*) as resulting from the horizontal cell-driven suppression of the sustained response in the intermediate ON pathway, which in turn is inherited from the modulation of the sustained cone response. Thus, even a circuit as simple as the one formulated in our model allows for a sustained modulation in the outer retina to be reflected in a transient modulation of a retinal output. A second interesting example relates to the asymmetry in response properties between intermediate ON and OFF pathways (Figure 7E). This asymmetry originates in the asymmetry of the cone response to light increments and decrements, which in turns relates to the adaptive nature of the cone response (Clark et al., 2013). In other words, light adaptation in cones translates into differential horizontal cell-driven modulations in ganglion cells.

Here, we show that in a circuit consisting of parallel channels with different temporal properties and non-linearities, the effect of a given circuit element on another circuit element can take qualitatively different forms, depending on the properties of the pathway connecting the two. Thus, a given interneuron type can affect the output channels of a brain region in various ways. Furthermore, we show that the way in which an interneuron influences another neuron that is multiple synapses away can be different from its local influence on the neurons it directly forms synapses with (in the case of horizontal cells, the cones). The computational model helped us to understand the effects due to the perturbation of an interneuron type in the retina; however, the employed processing principle—namely, the non-linear translation of a signal into parallel channels with different temporal properties—likely generalizes to other brain areas.

## STAR★METHODS

Detailed methods are provided in the online version of this paper and include the following:

- KEY RESOURCES TABLE
- CONTACT FOR REAGENT AND RESOURCE SHARING
- EXPERIMENTAL MODEL AND SUBJECT DETAILS
  - Animals
- METHOD DETAILS
  - Adeno-associated viruses (AAV)
  - AAV injections
  - Optimizing PSAM expression in horizontal cells

## SUPPLEMENTAL INFORMATION

Supplemental Information includes eight figures and three tables and can be found with this article online at https://doi.org/10.1016/j.neuron.2018.06.001.

## ACKNOWLEDGMENTS

We thank Z. Raics, N. Ledergerber, B. Gross-Scherf, C. Patino Alvarez, O. Keles, T. Szikra, P. Buchmann, R. Diggelmann, M. Fiscella, and J. Mueller for technical help; F. Muellner, S. Trenholm, A. Attinger, and C. Cowan for commenting on the manuscript; S. Sternson for PSAM-PSEM tools; and V. Gradinaru for the PHP.B serotype. This work was supported by the Boehringer Ingelheim Fonds (A.D.), the Swiss National Science Foundation (Sinergia Project CRSII3_141801 [R.A.d.S., B.R., and A.H.], Ambizione grant PZ00P3_167989 [F.F.], and NCCR "Molecular Systems Engineering" [B.R.]), the CNRS (UMR8559; R.A.d.S.), and the ERC (advanced grants 267351 "NeuroCMOS," 694829 "neuroXscales" [A.H. and F.F.], and 669157 "RETMUS" [B.R.]).

## AUTHOR CONTRIBUTIONS

A.D. designed the study, performed and analyzed microelectrode array and patch-clamp recordings, analyzed imaging data, performed viral injections and immunohistochemistry, and wrote the paper. F.F. designed the study, developed and implemented the computational model, analyzed microelectrode array and imaging data, performed hierarchical clustering, and wrote the paper. R.K.M. designed, performed, and analyzed imaging experiments; developed AAV; and performed viral injections. J.J. developed AAVs. D.H. wrote software for imaging analysis. P.H. built the initial version of setup used for microelectrode array recordings. A.H. guided the development of the microelectrode arrays. R.A.d.S. developed the computational model and wrote the paper. B.R. designed the study and wrote the paper.

## DECLARATION OF INTERESTS

The authors declare no competing interests.

Received: October 11, 2017
Revised: March 20, 2018
Accepted: June 1, 2018
Published: June 21, 2018

## REFERENCES

Applebury, M.L., Antoch, M.P., Baxter, L.C., Chun, L.L., Falk, J.D., Farhangfar, F., Kage, K., Krzystolik, M.G., Lyass, L.A., and Robbins, J.T. (2000). The murine cone photoreceptor: a single cone type expresses both S and M opsins with retinal spatial patterning. Neuron *27*, 513–523.

Baden, T., Berens, P., Franke, K., Román Rosón, M., Bethge, M., and Euler, T. (2016). The functional diversity of retinal ganglion cells in the mouse. Nature *529*, 345–350.

Burton, G.J., and Moorhead, I.R. (1987). Color and spatial structure in natural scenes. Appl. Opt. *26*, 157–170.

Chapot, C.A., Euler, T., and Schubert, T. (2017). How do horizontal cells 'talk' to cone photoreceptors? Different levels of complexity at the cone-horizontal cell synapse. J. Physiol. *595*, 5495–5506.

Chaya, T., Matsumoto, A., Sugita, Y., Watanabe, S., Kuwahara, R., Tachibana, M., and Furukawa, T. (2017). Versatile functional roles of horizontal cells in the retinal circuit. Sci. Rep. *7*, 5540.

Clark, D.A., Benichou, R., Meister, M., and Azeredo da Silveira, R. (2013). Dynamical adaptation in photoreceptors. PLoS Comput. Biol. *9*, e1003289.

Cook, P.B., and McReynolds, J.S. (1998). Lateral inhibition in the inner retina is important for spatial tuning of ganglion cells. Nat. Neurosci. *1*, 714–719.

Cronin, T., Vandenberghe, L.H., Hantz, P., Juttner, J., Reimann, A., Kacsó, A.-E., Huckfeldt, R.M., Busskamp, V., Kohler, H., Lagali, P.S., et al. (2014). Efficient transduction and optogenetic stimulation of retinal bipolar cells by a synthetic adeno-associated virus capsid and promoter. EMBO Mol. Med. *6*, 1175–1190.

Dalkara, D., Byrne, L.C., Klimczak, R.R., Visel, M., Yin, L., Merigan, W.H., Flannery, J.G., and Schaffer, D.V. (2013). In vivo-directed evolution of a new adeno-associated virus for therapeutic outer retinal gene delivery from the vitreous. Sci. Transl. Med. *5*, 189ra76.

Deverman, B.E., Pravdo, P.L., Simpson, B.P., Kumar, S.R., Chan, K.Y., Banerjee, A., Wu, W.L., Yang, B., Huber, N., Pasca, S.P., and Gradinaru, V. (2016). Cre-dependent selection yields AAV variants for widespread gene transfer to the adult brain. Nat. Biotechnol. *34*, 204–209.

Dupé, V., Davenne, M., Brocard, J., Dollé, P., Mark, M., Dierich, A., Chambon, P., and Rijli, F.M. (1997). In vivo functional analysis of the Hoxa-1 3′ retinoic acid response element (3'RARE). Development *124*, 399–410.

Farrow, K., Teixeira, M., Szikra, T., Viney, T.J., Balint, K., Yonehara, K., and Roska, B. (2013). Ambient illumination toggles a neuronal circuit switch in the retina and visual perception at cone threshold. Neuron *78*, 325–338.

Fiscella, M., Farrow, K., Jones, I.L., Jäckel, D., Müller, J., Frey, U., Bakkum, D.J., Hantz, P., Roska, B., and Hierlemann, A. (2012). Recording from defined populations of retinal ganglion cells using a high-density CMOS-integrated microelectrode array with real-time switchable electrode selection. J. Neurosci. Methods *211*, 103–113.

Franke, F., Quian Quiroga, R., Hierlemann, A., and Obermayer, K. (2015). Bayes optimal template matching for spike sorting - combining fisher discriminant analysis with optimal filtering. J. Comput. Neurosci. *38*, 439–459.

Franke, K., Berens, P., Schubert, T., Bethge, M., Euler, T., and Baden, T. (2017). Inhibition decorrelates visual feature representations in the inner retina. Nature *542*, 439–444.

Gollisch, T., and Meister, M. (2010). Eye smarter than scientists believed: neural computations in circuits of the retina. Neuron *65*, 150–164.

Jackman, S.L., Babai, N., Chambers, J.J., Thoreson, W.B., and Kramer, R.H. (2011). A positive feedback synapse from retinal horizontal cells to cone photoreceptors. PLoS Biol. *9*, e1001057.

Kramer, R.H., and Davenport, C.M. (2015). Lateral inhibition in the vertebrate retina: the case of the missing neurotransmitter. PLoS Biol. *13*, e1002322.

Liu, X., Hirano, A.A., Sun, X., Brecha, N.C., and Barnes, S. (2013). Calcium channels in rat horizontal cells regulate feedback inhibition of photoreceptors through an unconventional GABA- and pH-sensitive mechanism. J. Physiol. *591*, 3309–3324.

Magnus, C.J., Lee, P.H., Atasoy, D., Su, H.H., Looger, L.L., and Sternson, S.M. (2011). Chemical and genetic engineering of selective ion channel-ligand interactions. Science *333*, 1292–1296.

Mangel, S.C. (1991). Analysis of the horizontal cell contribution to the receptive field surround of ganglion cells in the rabbit retina. J. Physiol. *442*, 211–234.

Masland, R.H. (2012). The neuronal organization of the retina. Neuron *76*, 266–280.

Miller, R.F., and Dacheux, R.F. (1983). Intracellular chloride in retinal neurons: measurement and meaning. Vision Res. *23*, 399–411.

Müller, J., Ballini, M., Livi, P., Chen, Y., Radivojevic, M., Shadmani, A., Viswam, V., Jones, I.L., Fiscella, M., Diggelmann, R., et al. (2015). High-resolution CMOS MEA platform to study neurons at subcellular, cellular, and network levels. Lab Chip *15*, 2767–2780.

Peichl, L., and González-Soriano, J. (1994). Morphological types of horizontal cell in rodent retinae: a comparison of rat, mouse, gerbil, and guinea pig. Vis. Neurosci. *11*, 501–517.

Seung, H.S. (2002). Amplification, attenuation, and integration. Handb. Comput. Neurosci. 6–10.

Siegert, S., Cabuy, E., Scherf, B.G., Kohler, H., Panda, S., Le, Y.Z., Fehling, H.J., Gaidatzis, D., Stadler, M.B., and Roska, B. (2012). Transcriptional code and disease map for adult retinal cell types. Nat. Neurosci. *15*, 487–495, S1–S2.

Ströh, S., Puller, C., Swirski, S., Hölzel, M.-B., van der Linde, L.I.S., Segelken, J., Schultz, K., Block, C., Monyer, H., Willecke, K., et al. (2018). Eliminating glutamatergic input onto horizontal cells changes the dynamic range and receptive field organization of mouse retinal ganglion cells. J. Neurosci. *38*, 2015–2028.

Szikra, T., Trenholm, S., Drinnenberg, A., Jüttner, J., Raics, Z., Farrow, K., Biel, M., Awatramani, G., Clark, D.A., Sahel, J.-A., et al. (2014). Rods in daylight act as relay cells for cone-driven horizontal cell-mediated surround inhibition. Nat. Neurosci. *17*, 1728–1735.

Thoreson, W.B., and Mangel, S.C. (2012). Lateral interactions in the outer retina. Prog. Retin. Eye Res. *31*, 407–441.

Tikidji-Hamburyan, A., Reinhard, K., Seitter, H., Hovhannisyan, A., Procyk, C.A., Allen, A.E., Schenk, M., Lucas, R.J., and Münch, T.A. (2015). Retinal output changes qualitatively with every change in ambient illuminance. Nat. Neurosci. *18*, 66–74.

Viney, T.J. (2010). The diverse roles of inhibition in identified neural circuits. PhD thesis (University of Basel).

# STAR★METHODS

## KEY RESOURCES TABLE

| REAGENT or RESOURCE | SOURCE | IDENTIFIER |
|---|---|---|
| Antibodies | | |
| Rabbit anti-cone arrestin primary antibody | Millipore | Cat# AB15282; RRID: AB_11210270 |
| Rat anti-GFP primary antibody | Nacalai Tesque | Cat# 04404-84; RRID: AB_10013361 |
| Guinea pig anti-RBPMS primary antibody | Phospho Solution | Cat#1832-RBPMS; RRID: AB_2492226 |
| Rabbit anti-GFP primary antibody | Life Tech | Cat #A-11122; RRID: AB_221569 |
| Goat anti-ChAT primary antibody | Millipore | Cat# ab144P; RRID: AB_11214092 |
| Mouse anti-calbindin primary antibody | Swant | Code 300 |
| Alexa fluor 647 donkey anti-mouse secondary antibody | Thermo Fisher Scientific | Cat# A-31571; RRID: AB_162542 |
| Alexa fluor 633 donkey anti-rabbit secondary antibody | Invitrogen | Cat# A-31573; RRID: AB_2536183 |
| Alexa fluor 488 donkey anti-rabbit secondary antibody | Life technologies | A-21206; RRID: AB_2535792 |
| Alexa fluor 488 donkey anti-guinea pig secondary antibody | Jackson | Cat# 706-545-148; RRID: AB_2340472 |
| Alexa fluor 488 donkey anti-rat secondary antibody | Life technologies | Cat# A-21208; RRID: AB_2535794 |
| α-bungarotoxin, Alexa fluor 555 conjugate antibody | Thermo Fisher Scientific | Cat# B35451; RRID: AB_2617152 |
| Streptavidin, Alexa fluor 555 conjugate antibody | Thermo Fisher Scientific | S-32355; RRID: AB_2571525 |
| Hoechst 33342 | Thermo Fisher Scientific | Cat# H1399 |
| Neurobiotin tracer | Vector Laboratories | Cat# SP-1120, RRID: AB_2313575 |
| Bacterial and Virus Strains | | |
| AAV PHP.B Ef1a-DIO-PSAM | This paper | N/A |
| AAV BP2 ProA1-GCaMP6s | This paper | N/A |
| AAV 7m8 ProA5-DIO-PSAM | This paper | N/A |
| Chemicals, Peptides, and Recombinant Proteins | | |
| Isoflurane (Attane) | Provet | N/A |
| PSEM 308 | Apex Scientific | N/A |
| NBQX | Tocris Bioscience | Cat# 0373 |
| Experimental Models: Organisms/Strains | | |
| Mouse: Bl6 (strain: C57BL/6J) | Jackson laboratories | RRID: IMSR_JAX:000664 |
| Mouse: *R26*$^{NZG}$ FVB.Cg-Gt(Rosa)26SorTm1(CAG-lacZ-EFGP)Glh | Jackson laboratories | RRID: IMSR_JAX:012429 |
| Mouse: *PV-FlpO* (strain: B6.Cg-Pvalbtm2.1(FLPo)Hze/J) | Jackson laboratories | RRID: IMSR_JAX:022730 |
| Mouse: *Gja10Cre* (strain TGN-B6CF1 BAC-Gja10-Cre-F14) | Siegert et al., 2012; Szikra et al., 2014 | N/A |
| Mouse: *PVCre* (strain: B6.129P2-Pvalbtm1Arbr/J, RRID: IMSR_JAX:017320) | S. Arber, FMI Basel | N/A |
| Mouse: *CMV-Cre* | Dupé et al., 1997 | N/A |
| Oligonucleotides | | |
| Promoter ProA1, see Table S2 | This paper | N/A |
| Promoter ProA5, see Table S2 | This paper | N/A |
| Recombinant DNA | | |
| Plasmid: pCAG-PSAM-IRES-GFP | Magnus et al., 2011 | N/A |
| Plasmid: pAAV-ef1a-DIO-ChR2-EYFP | Laboratory of Karl Deisseroth | N/A |
| Plasmid: pAAV-EF1a-GCaMP6s-WPRE | N/A | N/A |
| Plasmid: pAAV-Ef1a-DIO-PSAM | This paper | N/A |
| Plasmid: pAAV-ProA1-GCaMP6s | This paper | N/A |
| Plasmid: pAAV-ProA5-DIO-PSAM | This paper | N/A |

(*Continued on next page*)

*Continued*

| REAGENT or RESOURCE | SOURCE | IDENTIFIER |
|---|---|---|
| AAV serotype: PHP.B | Deverman et al., 2016 | N/A |
| AAV serotype: BP2 | Cronin et al., 2014 | N/A |
| AAV serotype: 7m8 | Dalkara et al., 2013 | N/A |
| Software and Algorithms | | |
| LabVIEW | National Instruments | RRID: SCR_014325 |
| MATLAB | MathWorks | RRID: SCR_001622 |
| Imaris | Bitplane | RRID: SCR_007370 |
| Python | Python Software Foundation | RRID: SCR_008394 |
| ZEN Black 2012 software | Zeiss | N/A |
| ImageJ | Fiji | RRID: SCR_003070 |
| Spike sorting algorithm | Franke et al., 2015 | N/A |
| Other | | |
| Electrophysiology setup for two-photon laser-targeted patch-clamp recordings | Farrow et al., 2013 | Custom |
| Microelectrode array setup | Fiscella et al., 2012 | Custom |
| CMOS-based microelectrode arrays | Müller et al., 2015 | N/A |
| Two-photon functional imaging setup | N/A | Custom |
| Zeiss LSM 720 confocal microscope | Zeiss | Cat# LSM 720 |
| Hamilton syringe Neuros Model 7000.5, 0.5 μL | Hamilton company | Cat# 65457-01 |
| MF-membrane 0.45 μm pore size, 13mm | Millipore | Cat# HAWP01300 |
| Liquid flow meter | Sensirion | Cat# SLJ-2000 |
| Switched valve controller VC-6 | Warner Instruments | VC-6 |

## CONTACT FOR REAGENT AND RESOURCE SHARING

Further information and requests for resources and reagents should be directed to and will be fulfilled by the Lead Contact, Botond Roska (botond.roska@iob.ch).

## EXPERIMENTAL MODEL AND SUBJECT DETAILS

### Animals

All animal procedures were approved by the Veterinary Department of the Canton of Basel-Stadt, following the standard ethical guidelines as stated in the European Communities Guidelines on the Care and Use of Laboratory Animals, 86/609/EEC. Adult mice (4-16 weeks old) of both sexes were used. Mice were housed in groups (max. five animals per cage) and maintained on a 12-hour light/dark cycle. Mice were kept in individually ventilated cages (Blue Line IVCs, Tecniplast) with nesting material (Plexx) and bedding (Lignocel BK8-15, Rettenmaier & Söhne GmbH & Co KG). Water and food pellets (KLIBA NAFAG irradiated rodent breeding diet 3302.PM.V20, Provimi Kliba AG) were provided *ad libitum*.

*Gja10Cre* (strain: TGN-B6CF1 BAC-Gja10-Cre-F14) is a BAC transgenic line developed in-house (Siegert et al., 2012; Szikra et al., 2014). *PVCre* mice (strain: B6.129P2-Pvalbtm1Arbr/J, RRID: IMSR_JAX:017320) were kindly provided by S. Arber, FMI Basel, and crossed with *Bl6* mice (strain: C57BL/6J, RRID: IMSR_JAX:000664). *PV-FlpO* mice (strain: B6.Cg-Pvalbtm2.1(FLPo)Hze/J, RRID: IMSR_JAX:022730) were purchased from Jackson laboratories. *Flp-GFP*-reporter mice, which were obtained by crossing the $R26^{NZG}$ mouse strain (FVB.Cg-Gt(Rosa)26SorTm1(CAG-lacZ-EFGP)Glh, RRID: IMSR_JAX:012429) with *CMV-Cre* deleter mice (Dupé et al., 1997) to remove Cre-dependence, were kindly provided by F. Rijli, FMI Basel. *Flp-GFP*-reporter mice were crossed with *PV-FlpO* and *Gja10Cre* mice to obtain triple transgenic *Gja10Cre* × *PV-Flp* × *Flp-GFP*-reporter mice.

## METHOD DETAILS

### Adeno-associated viruses (AAV)

AAV production was carried out according to standard protocols. Genome copy number titration was performed using real-time PCR (Applied Biosystems, TaqMan reagents). pAAV-Ef1a-DIO-PSAM was used to express PSAM (pharmacologically selective actuator

module, PSAM$^{L141F\ Y115F}$-GlyR) (Magnus et al., 2011) in Cre-expressing horizontal cells. To obtain pAAV-Ef1a-DIO-PSAM, PSAM was PCR-amplified from pCAG-PSAM-IRES-GFP (kindly provided by S. Sternson, Janelia Research Campus) and sub-cloned into pAAV-ef1a-DIO-ChR2-EYFP (kindly provided by K. Deisseroth, Stanford University) using AscI/NheI sites. pAAV-ProA1-GCaMP6s was used to target the calcium indicator GCaMP6s to cones. ProA1 (sequence shown in Table S3) is a cone-specific promoter, which is part of a large-scale AAV promoter screen (Jüttner et al., unpublished data). pAAV-ProA5-DIO-PSAM was used to target PSAM to Cre-expressing ganglion cells. ProA5 (sequence shown in Table S3) is a ganglion cell specific promoter. pAAV-ProA5-DIO-PSAM was produced by replacing the promoter in pAAV-Ef1a-DIO-PSAM.

### AAV injections

Injections were performed in mice anesthetized with 2.5% Attane Isoflurane. To infect horizontal cells, AAVs (viral titer between $1 \times 10^{14}$ and $9 \times 10^{14}$ GC/ml) coated with the PHP.B capsid (Deverman et al., 2016) were administered systemically by injecting AAV intravenously via retro-orbital injections. A syringe (BD Micro-Fine insulin syringe 0.5 ml, 30G) was front-loaded with 30 µl AAV solution in PBS (phosphate buffered saline). The AAV solution was prepared such that at least $3.3 \times 10^{11}$ viral particles were injected per gram of mouse. The injection needle was positioned behind the globe of the eye, in the retro-orbital sinus coming from the nasal side. Retinas were collected 4-5 weeks after injection. Before the systemic AAV administration was established, horizontal cells were infected by injecting serotype-BP2 (Cronin et al., 2014) AAV (viral titer $2 \times 10^{14}$ GC/ml) into the subretinal space as described previously (Szikra et al., 2014). Since systemic administration using the PHP.B capsid is not efficient to infect cones (Deverman et al., 2016), subretinal injections of serotype-BP2 AAV (viral titer $7 \times 10^{12}$ GC/ml) were carried out to infect cones. Retinas were collected 3-5 weeks after injection. To infect ganglion cells, intravitreal injections of serotype-7m8 (Dalkara et al., 2013) AAV were performed. 2 µl of serotype-7m8 AAV solution (viral titer $7 \times 10^{13}$ GC/ml) was front-loaded into a blunt 5 µl Hamilton syringe and injected into the vitreous. To maximize infection of ganglion cells, a second injection was performed after 2-7 days. Retinas were collected 10-12 weeks after injection.

### Optimizing PSAM expression in horizontal cells

We tested eight AAVs with different serotypes, promoters and coding sequences to optimize PSAM expression in the retinas of *Gja10Cre* mice. PSAM expression was visualized by staining the fixed retina with α-bungarotoxin conjugated to Alexa-555 (Thermo Fisher, B35451, 2 mg/ml). Only weak expression was obtained after subretinal injections of pAAV-EF1a-DIO-EGFP-T2A-PSAM coated with serotype 2/8, pAAV-EF1a-DIO-PSAM-IRES-EGFP coated with serotype 2/8, pAAV-EF1a-DIO-EGFP-T2A-PSAM coated with serotype 2/8 or serotype BP2, and pAAV-EF1a-DIO-PSAM coated with serotype 2/8. Subretinal injections of pAAV-CBA-FLEX-GFP-T2A-PSAM coated with serotype 2/8 led to degeneration of photoreceptor outer segments. Intravenous injection of pAAV-Ef1a-DIO-PSAM coated with the PHP.B capsid and subretinal injection of pAAV-Ef1a-DIO-PSAM coated with serotype BP2 led to retina-wide, strong PSAM expression in horizontal cells (Figures 1 and S1).

### Preparation of retina for physiology

Light-adapted mice were deeply anesthetized with Attane Isoflurane and killed by decapitation. Retinas were isolated under dim red-light illumination in oxygenated Ringer's medium. For imaging experiments and targeted single-cell recordings, retinas were mounted ganglion-cell-layer-up on filter paper (MF-membrane 0.45 µm pore size, Millipore) with a $3 \times 2$ mm$^2$ aperture to allow for light stimulation of the photoreceptors. The ventral part of the retina was placed over the aperture. For microelectrode array recordings, a $3 \times 3$ mm$^2$ patch was cut from the ventral part of the retina and placed ganglion-cell-layer-down on the array. To secure the retina, a polyamid mesh (opening size 200 µm, thickness 100 µm) was lightly pressed against the tissue. During all physiological experiments, the retina was kept at 35°C and continuously superfused with oxygenated Ringer's medium bubbled for the duration of the experiment (max. 6 hours).

### Administration of the chemogenetic ligand PSEM

The pharmacologically selective effector molecule (PSEM) was bath-applied during physiological experiments. In pilot experiments, application of an initial version of PSEM (PSEM$^{89S}$, kindly provided by S. Sternson, Janelia Research Campus) at a concentration of 30 µM led to increased spiking activity of ganglion cells in control retinas. We therefore used a different version of PSEM, PSEM$^{308}$ (Apex Scientific), bath-applied at 3 µM throughout the study. 3 µM PSEM$^{308}$ did not show any significant off-target effects in control retinas, neither on GCaMP6s signals in cone axon terminals (Figures 2C–2F), nor on the spiking responses of ganglion cells (Figure S2D). PSEM was applied and washed out for 12 min at a perfusion rate of 1.8 ml/min, which was monitored using a liquid flow meter (SLJ-2000, Sensirion). Switching between Ringer's solution and PSEM$^{308}$ solution was controlled by a switched valve controller (VC-6, Warner Instruments).

### Chemogenetic perturbation of horizontal cells

The chemogenetic channel we used, PSAM$^{L141F\ Y115F}$-GlyR (Magnus et al., 2011), is permeable to chloride. PSAM was highly expressed in horizontal cell somata and dendrites (Figures 1B–1F and S1), therefore it is expected that PSAM/PSEM clamps the membrane potential of horizontal cells to the equilibrium potential of chloride ($E_{Cl}$). This has two consequences: First, under PSAM/PSEM horizontal cell feedback is static since the membrane potential of horizontal cells is unmodulated by light. Second, under

PSAM/PSEM the amount of horizontal cell feedback is close to the amount of feedback that horizontal cells provide in darkness, since the $E_{Cl}$ of horizontal cells was estimated to be close to – but slightly more depolarized – than the horizontal cell dark membrane potential (Miller and Dacheux, 1983). Our data are consistent with this hypothesized action of PSAM/PSEM in horizontal cells. First, we show that PSAM/PSEM efficiently blocks the lateral inhibition from horizontal cells to cones (Figure 2), indicating that PSAM/PSEM prevents horizontal cells from responding to light. Second, PSAM/PSEM slightly decreased the baseline calcium levels of cones (Figure S8F), which is consistent with a slightly depolarized horizontal cell potential (Liu et al., 2013). Thus, while PSAM/PSEM does not directly interfere with the feedback mechanism of horizontal cells to cones, which likely involves multiple synaptic mechanisms (Kramer and Davenport, 2015), PSAM/PSEM leads to a static horizontal cell feedback, that is unmodulated by the input of cones and whose fixed value is close the feedback that horizontal cells provide in darkness. Future work could determine if interference with the horizontal cell feedback mechanism itself will yield to similar effects in the retinal output than the perturbation used in this study. Moreover, performing adjustable perturbations with spatial selectivity can be of interest to further investigate horizontal cell function.

### Calcium imaging of cone axon terminals

GCaMP6s-expressing cone axon terminals were imaged in a whole-mount preparation of the retina. The same cone axon terminals were imaged before, during, and after PSEM application and during subsequent application of NBQX (Tocris Bioscience, bath-applied at 10 μM). The two-photon imaging system was equipped with a Mai Tai HP two-photon laser (Spectra Physics) tuned to 920 nm, a 60 × water-immersion objective (Fluor, 1.0 NA, Nikon), and a 510/20 nm band pass emission filter. For light stimulation of the retina, a custom-built UV LED projector (Acer, LED 405 nm) was triggered by a TTL (transistor-transistor logic) signal synchronized with the end of each horizontal line scan. Light stimuli were exclusively presented during the fly-back period of the horizontal scanning mirror, after an initial 6.5 s period to allow for the retina to adapt to the scanning laser. Image acquisition was performed using custom-made software written in LabVIEW (National Instruments) developed by Z. Raics, acquiring images of 3 μm/pixel at a rate of 10 Hz.

Light stimulation was controlled via custom-made software written in Python developed by Z. Raics. The stimuli to measure lateral inhibition (Figure 2) consisted of three repetitions of a small (120 μm diameter) or large (3900 μm diameter) flashed, circular light spot (duration 2 s). The light intensity of the spot stimulus was 41.9 $\mu W/cm^2$, corresponding to $7.23 \times 10^4$ photoisomerizations per rod per second (R*/s, measured and computed as described previously; Farrow et al., 2013). The background light intensity was 0.079 $\mu W/cm^2$, corresponding to $1.37 \times 10^2$ R*/s. The stimuli to record the response dynamics of cones (Figures S8A–S8D) consisted of a sequence of spatially uniform light steps of increasing and decreasing contrasts (duration of each step 1.86 s; eight contrast steps: 0.5 0.65, 0.375, 0.75, 0.25, 0.875, 0.125, 1, 0; with 0 corresponding to $1.37 \times 10^2$ R*/s and 1 corresponding to $7.23 \times 10^4$ R*/s) (Figure S8A), or large (3900 μm diameter) flashed, circular light spot as used for Figure 2 (Figures S8B–S8D).

### Microelectrode array recordings

Electrical activity of ganglion cells was recorded by using CMOS-based microelectrode arrays as described before (Fiscella et al., 2012). In initial experiments, arrays with 11,011 electrodes were used (Fiscella et al., 2012). In most experiments, arrays had 26,400 platinum electrodes over an area of 3.85 × 2.1 $mm^2$, and a center-to-center electrode distance of 17.5 μm (Müller et al., 2015) (Figure S2B). Electrical activity was simultaneously recorded from an arbitrarily selectable and reconfigurable subset of 1,024 electrodes. High-density electrode configurations, which allowed for simultaneous recording of cells in two 400 × 400 $\mu m^2$ retinal areas at maximal electrode density, were selected. By monitoring the online spiking responses to a 75 μm diameter circular light spot, the stimulation area was centered on each electrode configuration by moving the stage via a joystick-controlled system (Scientifica).

For light stimulation of the retina, a custom-built projector (Acer K10, LEDs 395 and 505 nm) was used to generate stimuli at a refresh rate of 60 Hz. The light was focused on the microelectrode array by a camera lens (Nikon) and a 5 × objective lens (LMPlanFLN Olympus, NA 0.13) after passing a neutral density filter (ND20, Thorlabs) (Figure S2A). The size of the stimulation area was 2.5 × 1.9 $mm^2$. The retina was adapted to gray background light (0.0217 $mW/cm^2$, corresponding to $8.8 \times 10^4$ R*/s) for > 30 minutes before recording started.

### Visual stimulation during microelectrode array experiments

Light stimuli were controlled via custom-made software written in Python developed by Z. Raics. The sequence of spatially uniform light steps of increasing and decreasing contrasts (Figures 3, 4, 6, 8E, 8F, S3, S5, S7G, and S7H) started with gray background light and consisted of the eight light steps (duration 1.86 s; Figure S2C). The stimulus was repeated five times. Using

$$\text{Michelson contrast} = \frac{\text{Intensity}_{\text{after step}} - \text{Intensity}_{\text{before step}}}{\text{Intensity}_{\text{after step}} + \text{Intensity}_{\text{before step}}},$$

the stimulus consisted of the following contrast values: 11%, −25%, 33%, −50%, 55%, −75%, 77%, −99%.

The barcode stimulus (Figures 5, S6A, and S6B) was composed of a pattern of greyscale, vertical bars moving horizontally across the screen. The intensity profile of the bar pattern mimicked the 1/f distribution (f: spatial frequency) of light intensities of natural

scenes, in which lower spatial frequencies have larger amplitudes and higher spatial frequencies have smaller amplitudes. The bar pattern was generated by superimposing sine waves (spatial frequency: between 1/9600 - 1/120 1/μm in 1/9600 1/μm steps; amplitude: 1/spatial frequency; phase: pseudo-random value between −180 and 180 degrees). The background light intensity was $8.8 \times 10^4$ R*/s, the intensity ranged from $5.9 \times 10^2$ R*/s ('black') to $1.76 \times 10^5$ R*/s ('white'). The bar pattern moved horizontally across the screen at a constant speed of 864 μm/s. The length of the pattern (duration × speed) was 9600 μm. The bar pattern initially appeared at one side of the screen ('flying in'), then moved across the screen, and left the screen at the other side of the screen ('flying out'): this ensured that each cell was exposed to each horizontal pixel of the pattern at some point in time. The stimulus was repeated six times.

The stimulus to detect PSAM-expressing PV ganglion cells (Figure 5H) consisted of seven repetitions of a short (6 s duration) natural movie. Spatially uniform light steps were used to further classify PSEM-identified ganglion cells into PV1, PV5, and PV6 cells (Figures S6D–S6F), ranging from $5.9 \times 10^2$ R*/s ('black') to $1.76 \times 10^5$ R*/s ('white').

The stimulus to measure lateral inhibition in ganglion cells (Figures 8H and S8G) consisted of small (200 μm diameter) and large (2000 μm diameter) flashed, circular light spots of increasing contrasts ($1.76 \times 10^5$ R*/s, 33% Michelson contrast) and decreasing contrasts ($5.9 \times 10^2$ R*/s, −99% Michelson contrast). Stimuli were presented for 0.5 s, interleaved with 1 s gray background stimulation ($8.8 \times 10^4$ R*/s). The position of the small spots alternated pseudo-randomly among 100 positions rasterizing an area of $0.5 \times 0.5$ mm$^2$ large area with a distance of 50 μm. Small spots of both contrasts were presented pseudo-randomly five times at each position. Large spots of both contrasts were presented ten times, pseudo-randomly interleaved among the small spot presentations.

### Two-photon laser-targeted patch-clamp recordings

The recording setup for targeted single-cell recordings, which includes a Mai Tai HP two-photon laser (Spectra Physics), has been described before (Farrow et al., 2013). To target GFP-labeled cells in retinas of *Gja10Cre* × *PV-Flp* × *Flp-GFP*-reporter mice, the two-photon fluorescence image was overlaid on an infrared image acquired using a CCD camera. PV1, PV5, and PV6 cells were targeted by selecting GFP-labeled cells with large somata, and further recognized based on their previously described physiological properties (Farrow et al., 2013; Viney, 2010). Light stimulation was controlled via custom-made software written in Python. A digital light projector (V300X, NEC) generated light stimuli at a refresh rate of 75 Hz. The light was focused on the photoreceptor layer after passing a neutral density filter (Thorlabs, ND40). The background light intensity was set to $6.4 \times 10^4$ R*/s ('gray'), the intensity of the stimuli ranged from $9.1 \times 10^2$ R*/s ('black') to $1.3 \times 10^5$ R*/s ('white'). Spiking activity and inhibitory currents were recorded as described before (Farrow et al., 2013). Briefly, spike recordings were made in cell-attached mode with electrodes pulled to 3–5 MΩ resistance and filled with Ringer's solution. Whole-cell recordings were made in voltage-clamp mode with electrodes pulled to 5-7 MΩ resistance and filled with caesium-based intracellular solution (Farrow et al., 2013). Inhibitory currents ('inhibition') were recorded by voltage clamping the cell to 0 mV, the equilibrium potential of unselective cation channels.

### Immunohistochemistry

Whole-mount retinas and retinal sections were stained as described previously (Szikra et al., 2014). The 150 μm thick retinal sections were cut using a vibratome, after embedding the fixed retina in 3% agarose in PBS. The following sets of primary and secondary antibodies were used: (i) Primary: mouse anti-calbindin (Swant, Code 300, 1:1000); secondary: donkey anti-mouse IgG conjugated with Alexa-647 (Thermo Fisher, A31571) (Figure 1F). (ii) Primary: rabbit anti-cone arrestin (Millipore, AB15282, 1:200); secondary: donkey anti-rabbit IgG conjugated with Alexa-633 (Invitrogen, A31573) (Figure 1H). (iii) Primary: rat anti-GFP (Nacalai Tesque, 04404-84, 1:200); secondary: donkey anti-rabbit IgG conjugated with Alexa 488 (Life technologies, A21206) (Figure 1G). (iv) Primary: guinea pig anti-RBPMS (Phospho Solution, Cat #1832-RBPMS, 1:200); secondary: donkey anti-guinea pig IgG conjugated with Alexa 488 (Jackson, 706-545-148) (Figure 5E). (v) Primary: rabbit anti-GFP (Life Tech, A11122); secondary: donkey anti-rat IgG conjugated with Alexa 488 (Life technologies, A21208) (Figure 6C). The secondary antibodies were applied at a concentration of 1:200 for 4 hours. PSAM was stained with α-Bungarotoxin conjugated to Alexa-555 (Thermo Fisher, B35451, 2 mg/ml), neurobiotin filled cells were processed with streptavidin-Alexa-555 (Thermo Fisher, S32355, 1:1000), and nuclei were stained with Hoechst 33342 (Thermo Fisher, H1399, 1:200), together with the secondary antibodies.

### Confocal microscopy

Confocal images were acquired using a Zeiss LSM 700 laser-scanning confocal microscope equipped with a Fluar 5 × /0.25 M27 objective (Figure 1E), a Plan-Apochromat 10 × /0.45 objective (Figure S1), an EC Plan-Neofluar 40 × /1.30 Oil M27 objective (Figures 1C, 1D, 1F, 5E, 5F, 6C, S7A, S7C, and S7E), and a Plan-Apochromat 63 × /1.40 Oil DIC M27 objective (Figures 1B, 1G, and 1H). The overview image of the retina (Figure 1E) was acquired performing a 4 × 4 tile scan with the 5 × objective and online-stitched using the ZEN Black 2012 software (Zeiss). Confocal image stacks were processed using Imaris (Bitplane) and ImageJ (Fiji).

### Circuit model

We modeled the cone response in an extension of the phenomenological models presented in Clark et al. (2013) and Szikra et al. (2014), in which we added inhibitory horizontal cell feedback. The cone response was calculated as

$$\tau_c \frac{dr}{dt} = \alpha_c y(t) - [1 + \beta_c z(t)](r(t) + \varphi h(t)), \qquad \text{(Equation 1)}$$

where

$$r(t) = V(t) - V_{dark}, \quad \text{(Equation 2)}$$

$V(t)$ and $V_{dark}$ were the instantaneous and dark membrane potentials of the cone, respectively, $h(t)$ was the feedback signal from the horizontal cell, and $\alpha_c$, $\beta_c$, and $\varphi$ were numerical factors. The time-varying functions, $y(t)$ and $z(t)$, were related to the light input through linear convolutions, as

$$y(t) = \int_{-\infty}^{t} dt' K_y(t - t') I(t'), \quad \text{(Equation 3)}$$

$$z(t) = \int_{-\infty}^{t} dt' K_z(t - t') I(t'), \quad \text{(Equation 4)}$$

where $I(t)$ was the incident light intensity (or, more precisely, R*/s). A simple filter of the form

$$K_y(t) = \frac{t}{\tau_y} \frac{e^{-\frac{t}{\tau_y}}}{\tau_y} \quad \text{(Equation 5)}$$

yielded faithful fits to experimentally measured cone responses (Clark et al., 2013; Szikra et al., 2014). The second filter had a similar form but also contained a delayed component, as

$$K_z(t) = \gamma K_y(t) + (1 - \gamma) \frac{t}{\tau_z} \frac{e^{-t/\tau_z}}{\tau_z}, \quad \text{(Equation 6)}$$

where $\tau_z$ was larger than $\tau_y$, and $0 \leq \gamma \leq 1$ ensured proper normalization. Note that $\int_0^\infty dt' K_y(t - t') = 1$ for all filters. The horizontal cell response was modeled analogously to the cone response, as

$$\tau_h \frac{dh}{dt} = \alpha_h y_h(t) - [1 + \beta_h z_h(t)] h(t), \quad \text{(Equation 7)}$$

$$h(t) = V_h(t) - V_{h,\,dark}, \quad \text{(Equation 8)}$$

where $V_h(t)$ and $V_{h,\,dark}$ were the instantaneous and dark membrane potentials of the horizontal cells, respectively, $y_h(t)$ and $z_h(t)$ were the quantities analogous to $y(t)$ and $z(t)$ but received the cone potential, instead of the light intensity, as input. Equations 1 and 7 are coupled differential equations. The solution to the approximated system of equations, in which the parameters $\tau_c$ and $\tau_h$ have been set to 0, i.e.,

$$\alpha_c y(t) - [1 + \beta_c z(t)](r(t) + \varphi h(t)) = 0, \quad \text{(Equation 9)}$$

$$\alpha_h y_h(t) - [1 + \beta_h z_h(t)] h(t) = 0, \quad \text{(Equation 10)}$$

yielded good fits to the cone response. Furthermore, for the stimuli considered in this study, the parameter $\beta_h$ could be set to zero without appreciable degradation of the fits; for all simulations shown here, we set $\beta_h = 0$. Without loss of generality, we can then set $\varphi = 1$, and the simplified, coupled system now reads

$$r(t) = \frac{\alpha_c y(t)}{[1 + \beta_c z(t)]} - h(t), \quad \text{(Equation 11)}$$

$$h(t) = \alpha_h \int_{-\infty}^{t} dt' K_h(t - t') r(t'), \quad \text{(Equation 12)}$$

where

$$K_h(t) = \frac{t}{\tau_h} \frac{e^{-t/\tau_h}}{\tau_h}. \quad \text{(Equation 13)}$$

All the parameters of the outer retina component (Equations 11 and 12) of our circuit model were fit once to cone responses (Figure 1E in Szikra et al., 2014), and then kept unchanged for all simulations reported here. The fitted values were $\alpha_c = -9.602 * 10^{-6}$, $\beta_c = -1.148 * 10^{-5}$, $\gamma = 0.764$, $\alpha_h = 0.177$, $\tau_y = 50.6\ ms$, $\tau_z = 576.9\ ms$, $\tau_h = 371.0\ ms$. The data used to fit the model were recordings in retinal slices (Szikra et al., 2014), where we expected that an appreciable part of the horizontal cell feedback to cones was

absent, as compared to a whole-mount retina. As such, we expected that our fits underestimated the value of the parameter $\alpha_h$ for whole-mount retinas. Indeed, the larger value we used in our simulations, $\alpha_h = 0.792$, yielded good qualitative agreement with the ganglion cell recordings presented in this study. To model the effect of PSEM, we set $\alpha_h = 0$ which removed the horizontal cell feedback from the cone.

The activity in the inner retina pathways, $b_{p,k}(t)$, was modeled as a threshold-linear functional of the cone potential,

$$b_{p,k}(t) = \left\lfloor -1^k \left( \int_{-\infty}^{t} dt' K_p(t-t') V(t') - \theta_{p,k} \right) \right\rfloor, \quad \text{(Equation 14)}$$

where $p = 1, 2, 3$ labeled the pathway (fast, intermediate, slow), $k = 0$ for OFF pathways and $k = 1$ for ON pathways,

$$\lfloor x \rfloor = \begin{cases} 0, & x < 0 \\ x, & x \geq 0 \end{cases} \quad \text{(Equation 15)}$$

was a thresholding non-linearity, and $\theta_{p,k}$ acted as threshold. The details of the form of the filters, $K_p(t)$, did not influence the results qualitatively; $K_1$ represented a high-pass filter which took the derivative of the cone potential on the order of 1 ms; $K_2$ was a high-pass filter with a very low cut-off frequency, in effect removing the DC-component of the cone potential; $K_3$ passed on the cone potential, including its DC-component, downstream. We chose the forms

$$K_1(t) = \sin\left(\frac{\pi t}{\mu}\right) \frac{1}{\sqrt{2\pi}\sigma} e^{-\frac{1}{2}\left(\frac{t-\mu}{\sigma}\right)^2}, \quad with \quad \mu = 3ms, \quad \sigma = 1ms \quad \text{(Equation 16)}$$

$$K_2(t) = \frac{1}{\tau_2} e^{-\frac{t}{\tau_2}} - \frac{1}{c_2 \tau_2} e^{-t/(c_2 \tau_2)}, \; with \quad \tau_2 = 50ms, \quad \text{(Equation 17)}$$

$$K_3(t) = \frac{1}{\tau_3} e^{-t/\tau_3}, \; with \; \tau_3 = 100ms, \quad \text{(Equation 18)}$$

where $c_2$ was a large positive numerical factor. The threshold $\theta_{p,k}$ was non-zero in two cases: In the fast pathways $\theta_{1,k} = -1^k \cdot 0.1$ and in the slow pathways $\theta_{3,k} = -23.5$, where $-23.5$ was the cone potential (with horizontal cell feedback) in response to a constant gray stimulus with the same light intensity as the first contrast value of our stimulus. We note that this choice of parameters worked for the stimulus used in this study but may not work for other stimuli.

Finally, the input $I_g(t)$ to a model ganglion cell was computed as a weighted sum of the activity in the inner retina pathways,

$$I_g(t) = \sum_{p=1}^{3} \sum_{k=0}^{1} w_{g,p,k} b_{p,k}(t). \quad \text{(Equation 19)}$$

Here, $g = 1, \ldots, 7$ labeled the seven different simulated ganglion cells (*i–vii* in Figure 7E); for each of these, at most two of the 3 × 2 prefactors, $w_{g,p,k}$, were non-vanishing. The spike rate of a model ganglion cell was obtained as the thresholded, weighted sum of the input and a temporally coarse version of its derivative (Figure 7B),

$$R_g(t) = \left\lfloor (1-\alpha_g) I_g(t) + \alpha_g \left( \int_{-\infty}^{t} dt' K_g(t-t') I_g(t') \right) - \theta_g \right\rfloor, \quad \text{(Equation 20)}$$

where $K_g(t)$ was a biphasic filter similar in its form to $K_1(t)$. Hereafter, we provide the parameters for the seven simulated ganglion cells (*i-vii*); the threshold, $\theta_g$, was given as a multiple of the peak response to the largest contrast step, all $w_{g,p,k} = 0$ except when indicated otherwise, and $ON = 1$, $OFF = 0$. For the sake of readability, we omit the subscript $g$.

(*i*) $w_{2,ON} = 1$, $\alpha = 1$, $\theta_g = .3$;
(*ii*) $w_{2,ON} = 1$, $\alpha = 0$; $\theta_g = .1$;
(*iii*) $w_{2,ON} = 2$, $w_{3,ON} = 1$, $\alpha = 0$; $\theta_g = 0$;
(*iv*) + (v) $w_{1,OFF} = 3$, $w_{2,ON} = -1$, $\alpha = 1$, $\theta_g = 0$;
(*vi*) $w_{2,OFF} = 1$, $w_{3,OFF} = 10$, $\alpha = 0$, $\theta_g = -.1$;
(*vii*) $w_{1,ON} = 1$, $\alpha = 0$, $\theta_g = 0$.

The parameters of the inner retina component and ganglion cell component were chosen by hand, without systematic fitting to the data, with the aim of capturing the observed effects qualitatively. All simulations were computed with a 1 ms sampling interval.

## QUANTIFICATION AND STATISTICAL ANALYSIS

### Quantification of retinal infection

To quantify PSAM expression in retinas of *Gja10-Cre* mice injected with AAV Ef1a-DIO-PSAM, confocal stacks were acquired from stained whole-mount retinas using an EC Plan-Neofluar 40 × /1.30 Oil M27 objective. No PSAM-positive cells were observed outside the inner nuclear layer and outer plexiform layer (Figure 1B). Cells were counted manually on a maximum-intensity projection of the inner nuclear layer and the outer plexiform layer. Calbindin was used to mark horizontal cells. To quantify GCaMP6s expression in retinas of mice injected with AAV-ProA1-GCaMP6s (Figure 1H), confocal stacks were acquired from stained retinal slices using a Plan-Apochromat 63 × /1.40 Oil DIC M27 objective. Cells were counted manually across all retinal layers. Cone arrestin was used to mark cones. To quantify PSAM expression in retinas of *PV-Cre* mice injected with AAV-ProA5-DIO-PSAM (Figure 5E), confocal stacks were acquired from stained whole-mount retinas using an EC Plan-Neofluar 40 × /1.30 Oil M27 objective. Cells were counted manually across all retinal layers. RBPMS was used to mark ganglion cells.

### Automated segmentation of cone axon terminals

Cone axon terminals were automatically detected semi-online via custom-made software written in Python. The temporal sequence of two-photon images was averaged in time to yield a 2D image, which was subsequently smoothed by a Gaussian filter (sigma = 1 μm). The putative centers of the terminals were located by finding the local maxima on the smoothed image. Starting from each of these local maxima, the radius of a terminal was estimated by first growing a circular mask (starting radius 2 μm, limit radius 3 μm) and an annulus surrounding the circular mask with an area larger or equal to the area of the growing circular mask. The proportion of the average pixel intensities under the circular and annulus masks was calculated in each step. The radius of the terminal was defined as the radius of the circular mask at which the proportion of the circular/annulus average pixel intensities was maximal. Pixels under this circular region were thresholded using Otsu's method, and the contiguous set of pixel coordinates overlapping with the center of the circular region was used to extract the time series of the two-photon signal. Automatic detection of cone terminals was manually corrected if the detection of single terminals failed for two closely positioned terminals.

### Analysis of cone imaging data

Data analysis was performed offline using MATLAB (MathWorks). For each terminal, fluorescence values were computed as the mean of all pixels belonging to the terminal. The background fluorescence (mean of the 10% dimmest pixels of each image frame) was subtracted. The activity was expressed as ΔF/F, where F represents the baseline fluorescence (mean fluorescence of 1 s time window before stimulus onset). ΔF/F values of three stimulus repetitions were averaged. Terminals with noisy baseline fluorescence (difference of maximal and minimal baseline fluorescence > 2 ΔF/F) were excluded from the analysis.

The response amplitude (Figures 2D and 2J) was defined as the mean of the absolute ΔF/F values during the second half of the stimulation period.

The lateral inhibition index (LII) of cone terminals (Figures 2F and 2L) was defined as

$$\mathrm{LII} = \frac{R_S - R_L}{R_S + R_L},$$

where $R_S$ and $R_L$ denote the responses (mean of ΔF/F values in second half of stimulation period) to small and large spot stimuli. The LII in the non-PSEM condition was computed by averaging the LII before PSEM application and after PSEM washout.

The substance-induced change in LII (ΔLII; Figures 2M and 2N) was defined as

$$\Delta\mathrm{LII} = \mathrm{LII}_{\mathrm{substance}} - \mathrm{LII}_{\mathrm{non-substance}},$$

where, to quantify NBQX-induced effects, $\mathrm{LII}_{\mathrm{substance}}$ denotes the LII during NBQX application and $\mathrm{LII}_{\mathrm{non\text{-}substance}}$ denotes the LII before NBQX application (same as washout of PSEM); and, to quantify PSEM-induced effects, $\mathrm{LII}_{\mathrm{substance}}$ denotes the LII during PSEM application and $\mathrm{LII}_{\mathrm{non\text{-}substance}}$ denotes the LII in the non-PSEM condition. The fraction of cones with decreased lateral inhibition was defined as the fraction of cones with substance-induced difference of LII < 0.

To compare the measured ΔF/F signals to the model cone responses (Figures S8A–S8C), we estimated the calcium indicator decay time constant by fitting a decaying exponential to the response of the cone to the onset of the scanning laser. We estimated the half-decay to be 0.73 s. We then convolved the model cone potential (Figures S8A and S8B), or deconvolved the averaged cone responses (Figures S8C and S8D, using MATLAB's 'deconv' function) with this exponential.

We quantified the degree to which the cone responses were transient (Figure S8D) by computing the %-change of the average deconvolved cone response (Figure S8C) in the interval 200 to 500ms, *RA*, and in the interval 500 to 800ms, *RB*, after the contrast step for each cone individually (transiency index).

$$\text{transiency index} = 100\frac{R_A - R_B}{R_A}$$

The normalized baseline calcium level (Figures S8E and S8F) was computed by normalizing the baseline fluorescence to the non-PSEM condition. Only stable cones were included in this analysis; a cone was classified as stable if the baseline fluorescence after PSEM washout was not smaller than 50% and not larger than 150% of the baseline fluorescence before PSEM application.

### Analysis of microelectrode array data

Data were analyzed offline using MATLAB (MathWorks). Spikes were sorted automatically using a two-stage procedure that first identified spike templates for each neuron via mean-shift clustering and then classified each spike using template matching (Franke et al., 2015). We excluded cells using a two-step procedure. First, cells with a template waveform amplitude below 6* $\sigma_N$ on all electrodes, where $\sigma_N$ is the noise standard deviation, were excluded from the analysis. For each remaining cell, the number of electrodes on which the template amplitude surpassed the spike detection threshold ('active electrodes') was computed. Cells with a template amplitude below 8* $\sigma_N$ and with fewer than 15 active electrodes were also excluded from the analysis. The spatial location of a ganglion cell on the microelectrode array (Figure S5) was approximated to the spatial location of the electrode that recorded the largest signal from the cell.

To analyze the response to the sequence of spatially uniform light steps of increasing and decreasing contrast (Figures 3, 6, 8E, 8F, S7G, and S7H), data were averaged across stimulus repetitions; the first of the five stimulus repetitions was excluded from the analysis. The transient part of the on-response, the sustained part of the on-response, the rebound on-response, and the entire on-response ('all-on') were computed as the mean spike rate during the respective time window, averaged over the four positive contrast steps; for the transient part of the off-responses and the entire off-response ('all-off') the procedure was identical, except that the data were averaged over the four negative contrast steps. Only visually responsive and stable cells were included in the analysis: a cell was classified as visually responsive if its transient response to the maximal contrast was larger than 10 Hz; a cell was classified as stable if the transient part of the response after washout of PSEM was not smaller than 50% and not larger than 150% of the transient part of the response before PSEM application. Moreover, for each combination of the response polarity and the response time window, cells were excluded from the analysis if their mean spike rate during the respective time window before PSEM application was smaller than 2 Hz.

Cells were classified as ON cells (on off index > 0.5) or OFF cells (on off index < −0.5) based on their responses before PSEM application using

$$\text{on off index} = \frac{R_{ON} - R_{OFF}}{R_{ON} + R_{OFF}},$$

where $R_{ON}$ denotes the transient part of the on-response and $R_{OFF}$ denotes the transient part of the off-response. A transient OFF cell was classified as a cell with rebound on-response if its rebound on-response (spike rate during 0.5-1.5 s time window after light increments) before PSEM application was larger than 2 Hz.

The relative change of the response $(\Delta R)$ in PSEM versus non-PSEM conditions (Figures 3, 6, 8E, 8F, S7G, and S7H) was defined as

$$\Delta R = \frac{R_{PSEM} - R_{Non\text{-}PSEM}}{R_{Non\text{-}PSEM} + 1},$$

where $R_{PSEM}$ denotes the mean spike rate during PSEM application and $R_{Non\text{-}PSEM}$ denotes the mean spike rate in the non-PSEM condition (mean value of before PSEM application and after PSEM washout).

The fraction of cells with PSEM-affected responses in PSAM retinas and control retinas was computed using two thresholds

$$t_- = mean(\Delta R_{Control}) - 2 * s.d.(\Delta R_{Control})$$

$$t_+ = mean(\Delta R_{Control}) + 2 * s.d.(\Delta R_{Control}),$$

where $\Delta R_{Control}$ was measured in control retinas. Responses were classified as 'PSEM-suppressed' if $\Delta R < t_-$; responses were classified as 'PSEM-enhanced' if $\Delta R > t_+$.

The response range of a cell (Figures 4C, 4D, and 8A) was computed by normalizing the responses evoked by the four stimulus contrasts to the maximal response in the non-PSEM condition. The response range was then defined as the difference between the maximal and minimal normalized responses.

To classify cells in slow-responding and fast-responding cells (Figure 8E) the first time point at which the spike rate reached 50% of the maximal spike rate of the response ('time to half peak response') was computed. Cells were classified as fast-responding if the time to half peak response to the step of maximal contrast was less than 0.65 s.

The LII of ganglion cells (Figures 8H and S8G) was computed analogously to that of cones. Among the 100 different locations of the small spot, the location that elicited the most spikes was chosen to compute the response to the small spot for each ganglion cell. Positive contrast stimuli were evaluated for ON cells, negative contrast stimuli were evaluated for OFF cells. Only responsive cells were included in this analysis; a cell was classified as responsive if its mean spike rate in response to the small spot was larger than > 2Hz.

### Clustering of responses to barcode stimulus

To cluster ganglion cells according to their responses to the barcode stimulus, each cell's spike trains were converted into spike rate profiles using a 50 ms bin length. The responses of the six trials were averaged. The spike rate profiles were smoothed by convolution with a kernel of length 5 bins (250 ms), before computing the pairwise distances between all pairs of cells. The cells responded to the barcode stimulus with different temporal lags, depending on their receptive field locations. Therefore, the distance between each pair of cells was computed as one minus the peak of the normalized cross-correlation function between the spike rate profiles of the two cells. The distances were used to construct a pairwise distance matrix from which a hierarchical cluster tree was computed with MATLAB's 'linkage' function and the group average as a measure for cluster distance. The hierarchical cluster tree represented the data as an ordered sequence of merging steps between cells or clusters of cells with increasing distance between the merged clusters. This sequence starts with as many clusters as there are cells in the data (each cell is in its own cluster) and successively merges pairs of clusters until all cells are within a single cluster. To decide upon the numbers of clusters and when to stop the merging within this sequence, the number of clusters with at least 30 members, and the distance between the merged clusters were plotted versus the ordered sequence of merging steps. The merging was stopped at the point in the sequence where the distance between successive merging steps started to grow exponentially, and the number of clusters with at least 30 members showed a plateau. As the precise position of this point did not qualitatively influence the results, we selected a point where 30 clusters remained, following Baden et al. (2016).

The 30 clusters were ordered according to the polarity of the cells that they contained (clusters 1-12: dominated by ON cells, clusters 13-24: dominated by OFF cells, clusters 25-30: both ON and OFF cells) and by the number of cells per cluster. To plot the responses within each cluster (Figures 5B, 5C, and S6B), responses were aligned with respect to the cross-correlation with a randomly chosen cell in each cluster and ordered with respect to the correlation to the mean response across all cells of the cluster.

To test if the responses of the PSEM-identified PV1, PV5 and PV6 cells to the barcode stimulus (Figure 5I) were significantly different, we first computed the mean firing rate profile for each cell over all six trials (spike count histogram with 50 ms bin width, smoothed with a Gaussian kernel of 100 ms width). The dimensionality of all averaged firing rate profiles was reduced to k by principal-component analysis. One-way multivariate analysis of variance (MANOVA) was then performed in the reduced subspace. We performed the MANOVA on a range of different values for k: independent of the number of dimensions used, the *P*-value was always smaller than $10^{-6}$.

### Identification of ganglion cell types on microelectrode arrays

The identification of PV1, PV5, and PV6 cells on the microelectrode arrays in retinas of *PV-Cre* mice injected with AAVs conditionally expressing PSAM (Figures 5D–5H) was performed in two steps (Figure S6C). In a first step, chemogenetically labeled PV ganglion cells were identified by analyzing the spiking responses to short natural movies (seven repetitions), recorded before ('before'), during ('PSEM'), and after ('wash') PSEM application. The mean spike count across stimulus repetitions was computed for each of the three conditions. Additionally, the standard deviation of the mean of the spike count was estimated as the standard deviation over the mean spike counts of randomly chosen sets of five of the seven repetitions. Cells were classified as sensitive to PSEM if two conditions were met: (1) the mean of the 'PSEM' distribution was smaller than the mean of the 'before' distribution minus four times the standard deviation of the mean in the 'before' distribution, and (2) the mean of the 'PSEM' distribution was smaller than the mean of the 'wash' distribution minus four times the standard deviation of the mean in the 'wash' distribution.

In a second step, PV1, PV5, and PV6 cells were further categorized based on their previously described light responses (Farrow et al., 2013; Viney, 2010). PV1, PV5, and PV6 cells are the only PV ganglion cell types that respond strongly and reliably to large (2.5 × 1.9 $mm^2$), spatially uniform stimuli (Farrow et al., 2013; Viney, 2010). We focused on PV1, PV5, and PV6 cells by selecting the chemogenetically labeled cells which showed strong and reliable responses to large, spatially uniform stimuli and discarding the chemogenetically cells for which large stimuli evoked only weak responses (corresponding to the other PV-expressing ganglion cell types; Farrow et al., 2013; Viney, 2010). The three types were further differentiated based on the polarity of their responses (PV1 cells are ON cells, PV5 and PV6 cells are OFF cells) and the temporal modulation of their spiking activity (PV5 cells have low background firing and transient off-responses, PV6 cells have high background firing and sustained off-responses) (Figures S6C–S6F).

### Analysis of targeted single-cell recordings

Data were analyzed offline using MATLAB (Mathworks). Spikes were detected by thresholding. The spiking responses to the sequence of spatially uniform light steps of increasing and decreasing contrast (Figure 6) were analyzed as described for the data obtained with microelectrode arrays. Inhibitory currents ('Inhibition'; Figures 8C and 8D) were normalized to pre-stimulus levels (mean inhibition in 1 s time window before stimulus onset) for each trial. Data were averaged across stimulus repetitions. To quantify inhibition during the time window of the rebound on-response (0.5-0.8 s after stimulus onset), inhibition was normalized to the 'before' condition (Figure 8D).

### Statistical analysis

The following statistical tests were used: two-sided sign-test, Mann-Whitney U test, Fisher's exact test, one-way multivariate analysis of variance (MANOVA), one-way analysis of variance (ANOVA), two-sided paired t test, Kolmogorov-Smirnoff test. In the following figure panels, data points were outside axis limits and are not shown: four data points (Figure 2D); two data points (Figure 2J);

four data points (Figure 2N); one data point from an ON cell (Figure 8G). In box-plot representations of Figures 4D and 8H, bottom and top whiskers indicate minima and maxima of data points not considered as outliers; bottom and top of boxes indicate first and third quartiles; central line indicates the median; black crosses indicate outliers (more than 1.5 times the interquartile range away from the top or bottom of the box). The following notations were used: n.s.: $p >= 0.05$; *: $0.05 > p >= 0.01$, **: $0.01 > p >= 0.001$, ***: $p < 0.001$. s.e.m.: standard error of the mean; s.d.: standard deviation. Sample sizes were not pre-determined using statistical methods. We did not use randomization. Data collection and analysis were not performed blindly to the experimental conditions.

## DATA AND SOFTWARE AVAILABILITY

Requests for data and software should be directed to and will be fulfilled by the Lead Contact, Botond Roska (botond.roska@iob.ch).